RESEARCH ARTICLE SUMMARY

BIOCHEMISTRY

Mammals produce *cyclo*-octasulfur to suppress lipid peroxidation and ferroptosis

Uladzimir Barayeu†, Seiryo Ogata†, Tsuyoshi Takata†, Minkyung Jung† *et al.*

Full article and list of author affiliations: https://doi.org/10.1126/science.aec5473

INTRODUCTION: Elemental sulfur is a central intermediate in the global sulfur cycle and is widely produced by prokaryotes, with additional evidence for its use in plants and fungi. Whether mammals synthesize, store, or use elemental sulfur, however, has remained unknown. Because mammalian cells enzymatically generate diverse reactive sulfur species, including hydropersulfides and polysulfides, we asked whether they also produce *cyclo*-octasulfur (S_8), the most stable allotrope of elemental sulfur, for biological function.

RATIONALE: We reasoned that if mammals use elemental sulfur as a biologically meaningful metabolite, S_8 should be maintained not as an incidental chemical product but as a regulated intracellular reservoir coupled to reactive sulfur metabolism. To test this possibility, we established complementary approaches: mass spectrometry using a polyaromatic capsule that captures and stabilizes S_8, enabling its quantitative analysis, and Raman microscopy for the direct visualization of S_8 in mammalian cells and tissues.

RESULTS: In line with established knowledge, we detected S_8 in bacteria and yeast and further found it in mammalian mitochondria and lipid droplets from mouse and human cells and tissues. S_8 was especially enriched in lipid droplets, corresponding by extrapolation to tens of grams or more of S_8 across the human body, with particularly high levels in adipocyte-rich breast cancer tissues. We identified lipid droplet–associated endothelial nitric oxide synthase (eNOS) as a major source of S_8. Recombinant eNOS converted glutathione polysulfides [e.g., glutathione trisulfide (GSSSG)] into longer sulfur chains and ultimately S_8 through an NADPH-dependent sulfur-catenation reaction, where NADPH is the reduced form of nicotinamide adenine dinucleotide phosphate; in the presence of glutathione polysulfides and the canonical eNOS substrate L-arginine, this reaction also generated the nitric oxide (NO) carrier *S*-nitrosoglutathione (GSNO). Functionally, depletion of endogenous S_8 increased lipid peroxidation and ferroptotic cell death, whereas S_8 delivery protected adipocytes and endothelial cells from ferroptosis. Mechanistically, S_8 reacted with abundant cellular thiols, such as glutathione (GSH), to generate antioxidant hydropersulfides and polysulfides that suppress lipid peroxidation. Local delivery of solubilized S_8 into joints of mice with experimental osteoarthritis also reduced lipid peroxidation in joint tissue, suggesting a potentially protective effect.

CONCLUSION: Our findings establish that mammalian cells not only synthesize elemental sulfur as S_8 but also sequester it within lipid-rich compartments at concentrations that surpass those of canonical lipophilic antioxidants such as vitamin E. This hydrophobic sulfur reservoir may provide a dynamic replenishment of redox-active persulfides, thereby linking sulfur-chain chemistry to eNOS-dependent signaling, the restraint of lipid peroxidation, and resistance to ferroptotic cell death. These results position elemental sulfur biosynthesis as an evolutionarily conserved yet metabolically adaptable antioxidant strategy, broadening the conceptual landscape of mammalian redox biology. □

Corresponding authors: Uladzimir Barayeu (barayeuu@mpip-mainz.mpg.de); Takaaki Akaike (takaaki.akaike.b4@tohoku.ac.jp) †These authors contributed equally to this work. **Cite this article as U. Barayeu *et al.*, *Science* 393, eaec5473 (2026). DOI: 10.1126/science. aec5473**

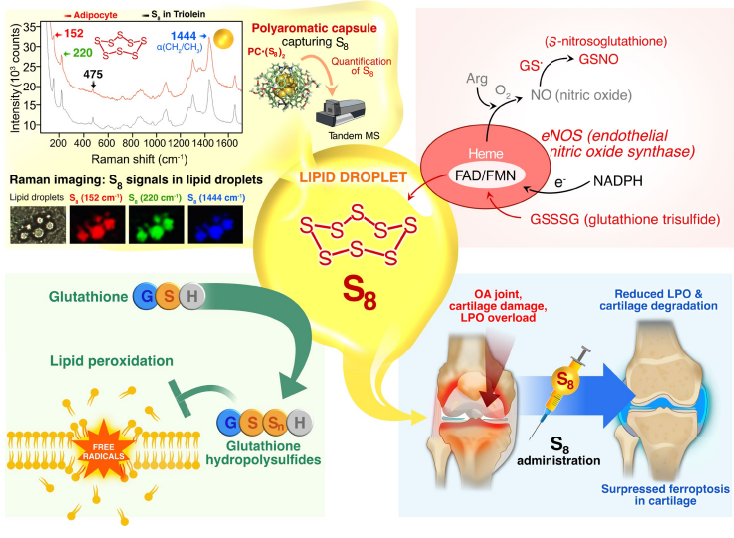

Mammalian biosynthesis of elemental sulfur. Complementary analytical approaches reveal S_8 in mammalian tissues and lipid droplets. eNOS-dependent sulfur catenation promotes S_8 formation, generating a lipid-associated sulfur pool that supplies hydropolysulfides to limit lipid peroxidation (LPO) and ferroptosis. Mobilization of this pathway may protect tissues from injury, including in osteoarthritis (OA). FAD, flavin adenine dinucleotide; FMN, flavin mononucleotide; MS, mass spectrometry; PC, polyaromatic capsule.

BIOCHEMISTRY

Mammals produce *cyclo*-octasulfur to suppress lipid peroxidation and ferroptosis

Uladzimir Barayeu[1,2]†*, Seiryo Ogata[1,2]†, Tsuyoshi Takata[1]†, Minkyung Jung[1]†, Tetsuro Matsunaga[1,3], Masanobu Morita[1,4], Tomoaki Ida[1], Mike Lange[5], Yuka Unno[1]‡, Saber Boushehri[2,6], Paulius Greicius[2,7], Akira Nishimura[8], Lorenzo Catti[9], Yuexuan Pan[1], Tianli Zhang[3], Takayuki Shimizu[10], Ryo Ushioda[11], Takakazu Nakabayashi[12], Seji Asamitsu[1,13], Kazuki Fusegawa[1,13], Takashi Suzuki[14], Takanori Ishida[15], Naoko Tanda[16], Yasuo Watanabe[17], Yukihiro Tsuchiya[17], Ryo Yamaguchi[18], Shintaro Noguchi[19], Eikan Mishima[4,20], Fumiko Yano[21], Mieko Arisawa[1,22], Dennis J. Stuehr[23], Ning Xia[24], Huige Li[24], Bernd Moosmann[25], Frauke Gräter[2,6], Camilo Aponte-Santamaría[6], James A. Olzmann[5], Marcus Conrad[1,20,26], Albert van der Vliet[1,27], Tobias P. Dick[28,29], Hozumi Motohashi[30], Michito Yoshizawa[9], Takaaki Akaike[1,18]*

Elemental sulfur is an evolutionarily ancient metabolite, yet its generation, storage, and function in animals have remained unclear. We show that mammals harbor elemental sulfur in the form of its most stable allotrope, *cyclo*-octasulfur (S_8). We found that S_8 accumulates to millimolar concentrations in mitochondrial membranes and in lipid droplets in both mouse and human cells. We further identified lipid droplet–associated nitric oxide synthase as a source of S_8 biosynthesis and found that S_8 accumulation in lipid droplets limits lipid peroxidation and suppresses ferroptosis. Accordingly, intra-articular injection of solubilized S_8 reduces lipid peroxidation in a mouse model of osteoarthritis. Together, these findings reveal an endogenous pool of S_8 in mammals that may protect cells from oxidative membrane damage by modulating cellular sensitivity to ferroptosis.

Life on Earth is thought to have emerged from hydrothermal vents (offering a rich source of sulfur) (*1*, *2*). Oxidative and reductive sulfur cycling are found in chemotrophic and phototrophic prokaryotes (*3*). Combined in microbial mats, these sulfur-cycling species form stromatolites, which are considered the oldest structured ecosystems on Earth (*4*). Elemental sulfur (S^0) is the predominant intermediate connecting sulfur-reducing and sulfur-oxidizing species in microbial mats and a redox hub in biogeochemical sulfur cycling (*4*–*6*). It is present in bacteria, archaea, algae, and plants (*5*–*8*). However, the role of elemental sulfur in eukaryotes is unclear (*6*, *8*), and it remains unknown whether mammals contain and metabolize elemental sulfur.

Recent advances in mass spectrometry (MS) have revealed sulfur-cycling intermediates—including hydrogen sulfide (H_2S) and hydropolysulfides (RSS_nH, where $n \geq 1$)—across the three domains of life (*9*, *10*). In mammalian cells, glutathione hydropersulfide (GSSH) can reach concentrations of up to 100 μM (*9*). In addition, RSS_nH have been implicated in cell signaling (*9*, *11*, *12*), energy metabolism (*10*), and antioxidant defense (*13*–*15*). Chemically, sulfur metabolites interconvert between thiols (RSH), disulfides (RSSH, R^1SSR^2), polysulfides (RSS_nH, $R^1SS_nR^2$), and elemental sulfur (*16*), raising the possibility that elemental sulfur is present in mammals.

We developed an MS-based approach and quantified elemental sulfur in the form of the most stable allotrope, *cyclo*-octasulfur (S_8) (*17*, *18*). This method, supported by Raman spectroscopy, enabled us to identify the presence of S_8 in mammalian cells. Consistent with the endosymbiotic theory, which posits that mitochondria may have originated from alphaproteobacteria capable of sulfur oxidation and reduction to and from elemental sulfur (*19*), we detected S_8 in mitochondria. Owing to its extreme hydrophobicity, S_8 is primarily localized in hydrophobic cellular environments, such as lipid droplets (LDs), which interface with mitochondria. We also identified endothelial nitric oxide (NO) synthase (eNOS) as an S_8-generating enzyme that facilitates the subsequent accumulation in LDs. Here, we propose that S_8 may serve as an evolutionarily conserved reservoir for reactive hydropolysulfides that support antioxidant defense in mammalian cells.

Results

Cyclo-octasulfur is a physiological metabolite present in mammals

We developed an MS-based method to measure elemental sulfur, using a polyaromatic capsule (PC) featuring a shape-defined hydrophobic cavity enclosed by a polyaromatic framework (*17*, *18*). This method relies on rapid encapsulation of S_8 by PC, driven by hydrophobic interaction and S-π interactions between S_8 and the polyaromatic shell. The polyaromatic shell of PC has a 4+ charge that facilitates detection of bound S_8 by MS (*17*), allowing us to establish a tandem mass spectrometry (MS/MS) technique for the absolute quantification of S_8 in aqueous solutions (figs. S1 to S5).

We validated measurement of S_8 in bacteria that accumulate S_8 in sulfur globules, such as *Allochromatium vinosum* and *Rhodobacter capsulatus* (*20*) (Fig. 1, A to C). In *R. capsulatus*, S_8 sulfur globule production was abolished by genetic ablation of sulfide:quinone oxidoreductase (SQR) (*21*), as demonstrated by phase contrast microscopy (Fig. 1B) and using the PC-based MS (Fig. 1C). Isolated sulfur globules from *R. capsulatus* also showed typical Raman bands for S_8 (fig. S6, A and B).

We detected S_8 in several organelles from human embryonic kidney 293T (HEK293T) cells, with higher concentrations in mitochondria than in endoplasmic reticulum (ER) or nuclear fractions (Fig. 1D and fig. S6C). S_8 accumulated in isolated mitochondria to a concentration of 3.8 mM. This intramitochondrial concentration was derived by integrating quantitative S_8 measurements from isolated HEK293T mitochondria (Fig. 1D) with independent estimates of mitochondrial volume. Moreover, mitochondria isolated from mouse embryonic fibroblasts (MEFs) derived from mitochondria-specific SQR-deficient mice (*22*) showed a partially decreased abundance of S_8 (fig. S6D). We also detected S_8 in *Schizosaccharomyces pombe* yeast, and removal of SQR again decreased abundance of S_8 (fig. S6E).

Given the hydrophobic nature of S_8, we expected its accumulation within hydrophobic cellular compartments, such as lipid membranes or LDs that are abundant in adipocytes. By both our PC method and the classical sulfane sulfur triphenylphosphine–based method for sulfane sulfur detection (*23*), we detected S_8 at millimolar concentrations in LDs isolated from differentiated mouse 3T3-L1 adipocytes (Fig. 1E). Further validation with Raman microscopy using LDs of differentiated 3T3-L1 adipocytes treated with sulfur donor glutathione trisulfide (GSSSG) revealed characteristic S_8 vibrations (152, 220, and 475 cm^{-1}) colocalized with characteristic α(CH_2/CH_3) vibrations from fatty acids [1444 cm^{-1} in LDs (*24*)] (Fig. 1, F and G, and fig. S7).

We also identified S_8 in white and brown adipose tissues of mice (Fig. 1H) and in LDs isolated from human breast and omental tissues (Fig. 1, I and J). Notably, concentrations of S_8 were much higher in cancerous breast tissues than in contralateral breast tissues from the same patients (Fig. 1I), exceeding 100 mM, as corroborated by Raman spectroscopy (fig. S6F). Quantification of sulfur-related metabolites in exhaled breath droplets (aerosols) from human breast cancer patients revealed significantly elevated inorganic polysulfides compared with levels in samples from healthy controls (fig. S8), consistent with our observation of high S_8 levels in cancerous breast tissues.

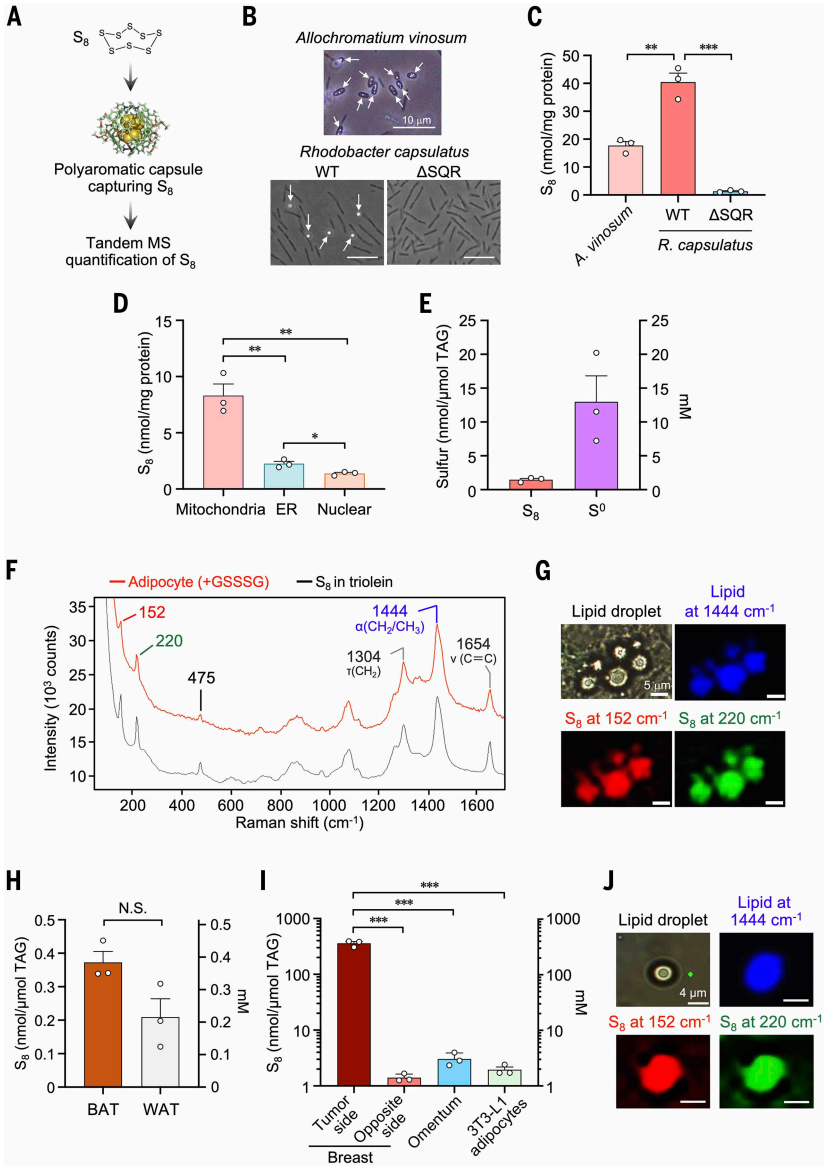

Fig. 1. Detection of S_8 in prokaryotes and eukaryotes. (**A**) Schematic of the workflow used to quantify S_8 with PC and MS/MS. (**B**) Phase-contrast micrographs showing intracellular sulfur globules in *A. vinosum* (top) and extracellular sulfur globules in *R. capsulatus* (bottom). Wild-type (WT) *R. capsulatus* produced sulfur globules, whereas the SQR-disrupted strain (ΔSQR) did not. Arrows indicate bacterial sulfur globules. Scale bars are 10 μm. (**C**) Quantification of S_8 in *A. vinosum* and in WT and ΔSQR *R. capsulatus* using PC. (**D**) Quantification of S_8 in mitochondrial, ER, and nuclear fractions isolated from HEK293T cells. S_8 accumulated in isolated mitochondria, reaching a concentration of 3.8 mM. (**E**) Quantification of S_8 and sulfane sulfur in LDs isolated from 3T3-L1 adipocytes. The right *y* axis indicates the amount of S_8 in LDs, calculated from the density of TAG. (**F**) Raman spectra of LDs from 3T3-L1 adipocytes treated with 3 mM GSSSG for 1 hour, showing peaks at 152, 220, and 475 cm^{-1} assigned to S_8 and peaks at 1304, 1444, and 1654 cm^{-1} assigned to LDs. (**G**) Raman images of 3T3-L1 adipocytes showing S_8 signals at 152 cm^{-1} (red) and 220 cm^{-1} (green) and the lipid signal at 1444 cm^{-1} (blue). Scale bars are 5 μm. (**H**) Quantification of S_8 in mouse brown adipose tissue (BAT) and white adipose tissue (WAT). The right *y* axis indicates the amount of S_8 in tissue LDs, converted to concentration using the density of TAG. (**I**) Quantification of S_8 in LDs isolated from human breast tissue with a tumor (tumor side) and contralateral breast tissue without a macroscopic tumor (opposite side) from the same patient, omental tissue from a patient with a gastrointestinal stromal tumor, and 3T3-L1 adipocytes. The right *y* axis indicates the amount of S_8 in human tissue LDs, converted to concentration using the density of TAG. For the tumor side, one sample was collected from each of four patients (patients 1 to 4; table S1). For the opposite side, three samples were collected from the contralateral breast of one patient (patient 1) with left breast cancer and a *BRCA* mutation. The omental sample was measured in three distinct regions, and 3T3-L1 adipocytes were analyzed in biological triplicate. (**J**) Raman imaging of S_8 in LDs from human breast tumor tissue. Scale bars are 4 μm. Data are means ± SD. $*P < 0.05$, $**P < 0.01$, $***P < 0.001$, and N.S. is not significant. Data were analyzed by Student's *t* test (H) or multiple *t* test [(C), (D), and (I)].

eNOS is a major source of S_8 biosynthesis

We investigated whether certain enzymes associated with LDs might contribute to S_8 biosynthesis. Heme proteins can catalyze elongation of sulfur chains in a process called catenation (*25*). Because differentiation of 3T3-L1 adipocytes is accompanied by increased expression of the heme-dependent enzyme eNOS (*26*) (fig. S9, A and B), we tested whether eNOS might drive S_8 accumulation in LDs. Proteome analysis of LDs isolated from 3T3-L1 adipocytes (Fig. 2A and fig. S9C) revealed the presence of eNOS and its associated protein caveolin-1. Intriguingly, S_8 levels in mouse adipocytes were elevated when eNOS

[1]Department of Redox Molecular Medicine, Tohoku University Graduate School of Medicine, Sendai, Japan. [2]Max-Planck-Institute for Polymer Research, Mainz, Germany. [3]Comprehensive Center for Infectious Disease Control, Graduate School of Medicine, Akita University, Akita, Japan. [4]Department of Environmental Medicine and Molecular Toxicology, Tohoku University Graduate School of Medicine, Sendai, Japan. [5]Departments of Molecular and Cell Biology and Metabolic Biology and Nutrition, University of California, Berkeley, Berkeley, CA, USA. [6]Heidelberg Institute for Theoretical Studies, Schloß-Wolfsbrunnenweg 35, Heidelberg, Germany. [7]Max Planck School Matter to Life, Heidelberg, Germany. [8]Department of Food and Agricultural Sciences, Faculty of Agriculture, Iwate University, Morioka, Iwate, Japan. [9]Laboratory for Chemistry and Life Science, Institute of Integrated Research, Institute of Science Tokyo, Yokohama, Japan. [10]Faculty Division of Natural Sciences, Nara Women's University, Nara, Japan. [11]Department of Molecular Biosciences, Faculty of Life Sciences, Kyoto Sangyo University, Kyoto, Japan. [12]Graduate School of Pharmaceutical Sciences, Tohoku University, Sendai, Japan. [13]Department of Surgery, Tohoku University Graduate School of Medicine, Sendai, Japan. [14]Department of Anatomic Pathology, Tohoku University Graduate School of Medicine, Sendai, Japan. [15]Department of Breast and Endocrine Surgical Oncology, Graduate School of Medicine, Tohoku University, Sendai, Japan. [16]Division of Preventive Dentistry, Graduate School of Dentistry, Tohoku University, Sendai, Japan. [17]Department of Pharmacology, Showa Pharmaceutical University, Machida, Japan. [18]Shimadzu × Tohoku University Supersulfides Life Science Co-creation Research Center, Sendai, Japan. [19]HORIBA, Ltd., Kyoto, Japan. [20]Institute of Metabolism and Cell Death, Molecular Targets and Therapeutics Center, Helmholtz Munich, Neuherberg, Germany. [21]Showa Medical University Research Administration Center, Showa Medical University, Tokyo, Japan. [22]Department of Bioscience and Biotechnology, Graduate School of Bioresource and Bioenvironmental Sciences, Kyushu University, Fukuoka, Japan. [23]Department of Inflammation and Immunity, Cleveland Clinic Research, The Cleveland Clinic, Cleveland, OH, USA. [24]Department of Pharmacology, University Medical Center, Johannes Gutenberg University, Mainz, Germany. [25]Evolutionary Biochemistry and Redox Medicine, Institute for Pathobiochemistry, University Medical Center of the Johannes Gutenberg University, Mainz, Germany. [26]Translational Redox Biology, Technical University of Munich (TUM), TUM Natural School of Sciences, Garching, Germany. [27]Department of Pathology and Laboratory Medicine, Robert Larner M.D., College of Medicine, University of Vermont, Burlington, VT, USA. [28]Division of Redox Regulation, DKFZ-ZMBH Alliance, German Cancer Research Center (DKFZ), Heidelberg, Germany. [29]Faculty of Biosciences, Heidelberg University, Heidelberg, Germany. [30]Department of Medical Biochemistry, Tohoku University Graduate School of Medicine, Sendai, Japan. ***Corresponding author. Email: barayeuu@mpip-mainz.mpg.de (U.B.); takaaki.akaike.b4@tohoku.ac.jp (T.A.)** †These authors contributed equally to this work. ‡Present address: Miyagi Cancer Center Research Institute, Division of Molecular and Cellular Oncology, Miyagi, Japan.

was overexpressed (Fig. 2B). Using Raman microscopy, we observed that adipocytes produce S_8 in the presence of the sulfur donor GSSSG upon activation of eNOS using the Ca^{2+} ionophore A23187, which was further enhanced by the eNOS overexpression (fig. S10A). Conversely, adipocyte S_8 levels were impaired in adipose tissues from mice in which eNOS was conditionally depleted in adipocytes (eNOS-CKO mice) (*27*), as compared with wild-type control mice (Fig. 2C).

Comparable findings were observed in human umbilical vein endothelial cells (HUVECs), which endogenously express eNOS (*28*, *29*) and in which eNOS was activated with A23187 (Fig. 2, D to G). eNOS activation also increased multiple sulfur-catenated species, including $CysSS_nH$, GSS_nH, and HSS_nH, in both eNOS-overexpressing HEK293T cells (fig. S11, A and B) and HUVECs (Fig. 2, D to F, and fig. S11C). The physiological relevance of Ca^{2+}-influx-driven, eNOS-dependent S_8 formation is supported by our recent study of angiogenesis and vascular function (*30*). In line with this, stimulation with vascular endothelial growth factor (VEGF) or bradykinin, both of which promote Ca^{2+}-driven activation of eNOS (*30*, *31*), increased S_8 formation in HUVECs (Fig. 2F). The role of eNOS in S_8 biosynthesis was further confirmed by observations of reduced S_8 levels in eNOS-depleted [knockdown (KD)] HUVECs, both in unstimulated and A23187-stimulated cells (Fig. 2G). Collectively, these studies support an important role for eNOS in LD- and adipocyte-associated S_8 production.

Imaging of mitochondria and LDs revealed spatial association between mitochondria and a fraction of LDs, suggesting a possible functional interaction of these organelles in S_8 metabolism in HUVECs (fig. S11, D to F). Some eNOS localized with LDs in HUVECs under baseline conditions, and the extent of such colocalization increased upon A23187 stimulation (Fig. 2H and fig. S11F), corresponding to increased S_8 production in these cells. Raman imaging confirmed S_8 localization in LDs in HUVECs (Fig. 2I and fig. S11G). When HUVECs were deprived of cystine, a precursor of cysteine and associated hydropolysulfides, they showed a less pronounced increase of S_8 upon Ca^{2+} ionophore stimulation than cells supplemented with 5 mM cysteine (CysSH), indicating that enhanced hydropolysulfide supply can promote cellular S_8 production mediated by eNOS (fig. S11H). This S_8-producing capacity was also confirmed in human vascular endothelial cells other than HUVECs (fig. S11I).

We performed mechanistic studies with recombinant eNOS, which was found to consume GSSSG at the expense of NADPH [reduced form of nicotinamide adenine dinucleotide phosphate ($NADP^+$)] even in the absence of eNOS-activating cofactor calmodulin (CaM) (*32*) (Fig. 3A). This reaction generated catenated sulfur species such as GSSSH, HSSH, and HSSSH, which is indicative of eNOS-dependent sulfur catenation (Fig. 3B and fig. S12A) and consistent with the sulfur metabolome in cells (Fig. 2E); this eventually resulted in accumulated production of S_8 (Fig. 3C and fig. S13A), which could be further enhanced by activation of eNOS with CaM (Fig. 3D). The addition of L-arginine did not influence S_8 production, indicating that eNOS operates through separate pathways for NO and S_8 production (Fig. 3D). Also, we observed increased NADPH consumption by eNOS when both L-arginine and GSSSG were present (Fig. 3E). Moreover, heme-binding NOS inhibitors L-NAME and L-NMMA (*33*) did not affect S_8 accumulation (Fig. 3F and fig. S13, B and C), whereas a flavoprotein inhibitor diphenyleneiodonium (DPI) (*34*) abolished S_8 formation (Fig. 3F and fig. S13D). Therefore, we propose distinct but catalytically integrated models of eNOS for S_8 biosynthesis (fig. S12B).

Comparisons of different glutathione polysulfides indicated that only GSSSG and GSSSSG (glutathione tetrasulfide) led to the formation of catenated sulfur species (figs. S13E; S14, A and B; and S15). Moreover, the enhancement of eNOS-mediated NADPH consumption requires a full glutathione (GSH) tripeptide base, which could not be substituted for cysteine or *N*-acetylcysteine trisulfides, indicating a critical dependence of specific interactions between GSH-based species and eNOS (fig. S14, C and D). Examining a panel of other trisulfides of tripeptides, we found that only GSSSG led to a consumption of NADPH, underscoring the substrate specificity of NOS (fig. S16, A and B).

The sulfur catenating activity of NOS strictly depended on NADPH, not NADH [reduced form of nicotinamide adenine dinucleotide (NAD^+)] (fig. S16C), and similar activity was observed with all three NOS isoforms (fig. S14E), demonstrating a conserved biochemical function shared by all NOS enzymes (*32*, *33*). Because NOS can produce superoxide, we examined whether superoxide could catenate sulfur chains independently of the enzymatic activity of NOS. However, no GSSSG catenation was observed in the presence of the superoxide-producing enzyme xanthine oxidase (XO), or other NAD(P)H-dependent oxidoreductases such as P450 reductase (P450R), NAD(P)H quinone dehydrogenase 1 (NQO1), or ferroptosis suppressor protein 1 (FSP1) (fig. S14F). These findings confirm that NOS is distinctively capable of using glutathione polysulfides, for catalyzing their reduction and catenating the sulfur chain.

We used AlphaFold3 to model the structure of the flavin adenine dinucleotide (FAD)–binding flavoprotein reductase–type domain of eNOS in complex with the ligands $FADH_2$ (reduced FAD), flavin mononucleotide (FMN), tetrahydrobiopterin (BH_4), and GSSSG. We identified structural models in which GSSSG comes in close proximity to $FADH_2$, which may enable direct transfer (fig. S17, A to C). But we also noted that in predictions where GSSSG is not directly close to $FADH_2$, electrons may be transferred indirectly via side chains of aromatic residues of eNOS (fig. S17D).

The inhibitory effect of DPI suggests that GSSSG may accept electrons from the NOS reductase domain, particularly from FAD. One-electron reduction of GSSSG would convert it to $GSSSG^{\bullet-}$, which subsequently decomposes to $GSS^{\bullet}$ and GS^- (*35*). Rapid combination of two molecules of $GSS^{\bullet}$ generates GSSSSG (*13*, *35*), thus catenating the sulfur chain by one sulfur atom. Because GSSSSG can also serve as a substrate, it may be reduced to $GSSSSG^{\bullet-}$, which decomposes, generating $GSSS^{\bullet}$ and GS^-, among other products. Similar reduction of GSSSSG could then lead to continuous catenation of the sulfur chain. Once a sulfur chain exceeds 10 atoms in length, it could be cyclized to produce the thermodynamically stable S_8, as a thermodynamic sink (Fig. 3G). The S_8 produced was stabilized and sequestered, and it accumulated in LDs, as shown by Raman analysis in fig. S18. The involvement of intermediate radical species could be corroborated by complete suppression of S_8 production by the spin trap 5,5-dimethyl-1-pyrroline *N*-oxide (DMPO) (Fig. 3H). When DMPO was added to the reaction, DMPO=S was detected in the GSSSG-eNOS reaction (fig. S14G), potentially originating from the decomposition of unstable DMPO-GSS_nSG radical adducts.

Addition of GSSSG to recombinant eNOS did not suppress its NO production but rather appeared to enhance it based on the increased accumulation of nitrite (Fig. 3I). In the presence of eNOS, L-arginine, and NADPH, GSSSG also facilitated the generation of *S*-nitrosoglutathione (GSNO) (Fig. 3J), which was enhanced with exogenously added LDs. Hence, the GSSSG-reducing activity of eNOS may present an additional mechanism of GSNO production within LDs, where radical coupling or redox-based reactions among hydrophobic reactive species—for example, NO, NO_2, and polysulfides and their perpolythiyl radicals—might be sustained (Fig. 3K).

S_8 protects against lipid peroxidation and ferroptosis

Upon differentiation of 3T3-L1 adipocytes, LDs accumulate (fig. S9B) and cells become resistant to ferroptosis induced by inhibitors of the cystine transporter (cystine/glutamate antiporter, system x_c^-) and glutathione peroxidase 4 (GPX4), such as erastin, sulfasalazine, Ras-selective lethal small molecule 3 (RSL3), and JKE-1674 (Fig. 4A and fig. S19, A and B). Likewise, the FSP1 inhibitor viFSP1 (*36*) failed to sensitize adipocytes to RSL3 (fig. S19C). Accumulation of S_8 in LDs might serve as a local reservoir for active persulfides that can potently inhibit lipid peroxidation (LPO) and may thereby prevent ferroptosis (*13*–*15*). To test this, we investigated the effect of endogenous S_8 on

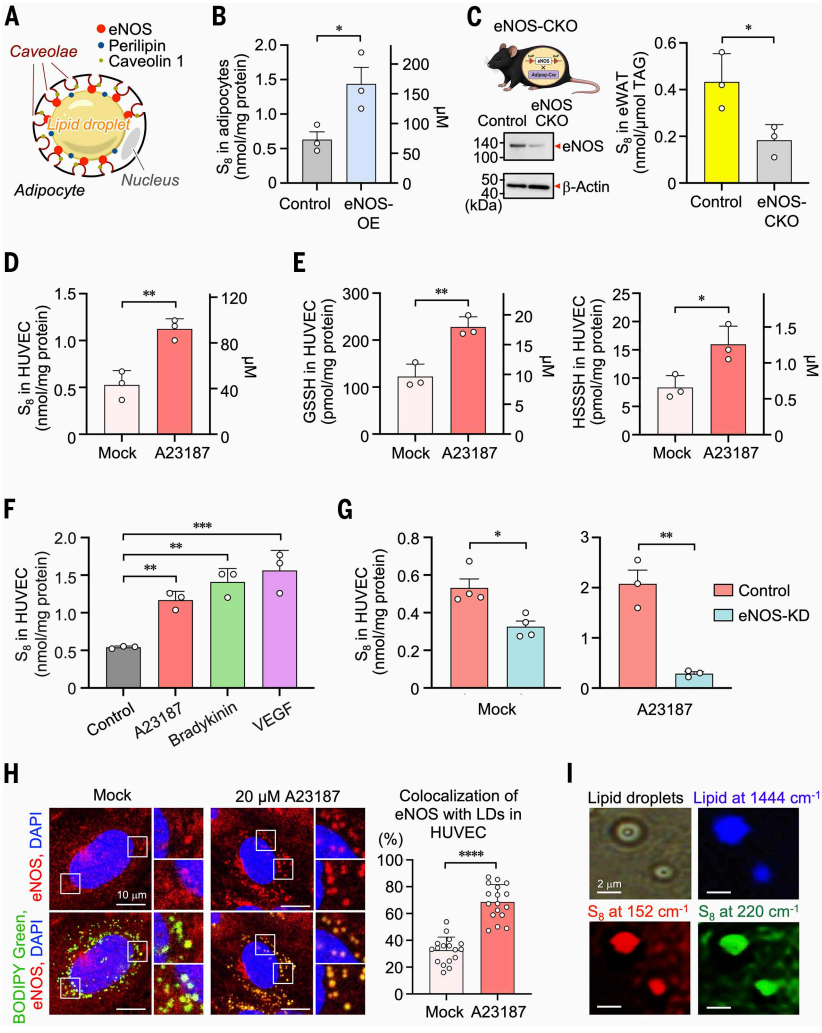

Fig. 2. eNOS-dependent S_8 production in LDs. (**A**) Schematic illustration of mammalian LDs showing the association of eNOS, perilipin, and caveolin-1. (**B**) Quantification of S_8 production in 3T3-L1 adipocytes transfected with empty vector (control) or an eNOS overexpression plasmid (eNOS-OE). (**C**) Generation of adipocyte-specific eNOS conditional knockout (i.e., conditional deletion) (eNOS-CKO) mice (top left) by crossing $eNOS^{flox}$ mice, in which exons 2 to 4 of the eNOS gene are flanked by loxP sites, with *Adipoq*-Cre transgenic mice expressing Cre recombinase under the control of the adiponectin promoter (*27*). Western blotting of endogenous eNOS expression in epididymal WAT (eWAT) from WT and eNOS-CKO mice (bottom left). Quantification of S_8 in eWAT from eNOS-CKO mice (right). (**D**) Quantification of S_8 production in HUVECs treated with A23187 (1 μM) for 5 min. The right *y* axis indicates the intracellular S_8 concentration, calculated from cell volume and protein content. (**E**) Quantification of GSSH (left) and HSSSH (right) in HUVECs treated with A23187 (1 μM) for 5 min. The right *y* axis indicates the intracellular concentration of each analyte, calculated from cell volume and protein content. (**F**) Quantification of S_8 production in HUVECs treated with A23187 (20 μM), bradykinin (10 μM), or VEGF (50 ng ml^{-1}) for the indicated times. A23187 and bradykinin were applied for 10 min, whereas VEGF was applied for 60 min. The indicated time points correspond to approximate peak values determined in preliminary time-course experiments. (**G**) Quantification of S_8 in eNOS-depleted (eNOS-KD) HUVECs treated with or without A23187. (**H**) Confocal fluorescence images showing colocalization of eNOS with LDs in HUVECs treated with or without A23187 (20 μM) for 10 min. Colocalization was assessed in 17 fields per condition, each containing more than 5 to 10 cells, with eNOS shown in red and LDs in green. Scale bars are 10 μm. (**I**) Raman imaging of S_8 in HUVECs after treatment with A23187 (20 μM) for 10 min. Scale bars are 2 μm. Data are means ± SD. $*P < 0.05$, $**P < 0.01$, $***P < 0.001$, and $****P < 0.0001$. Data were analyzed by Student's *t* test [(B) to (E), (G), and (H)] or one-way analysis of variance (ANOVA) with Tukey's test (F).

the protection against LPO and ferroptosis in adipocytes by depleting endogenous S_8 using PC (Fig. 4B and figs. S10, B to D, and S20). Indeed, S_8 depletion triggered LPO and cell death, which could be mitigated by the radical trapping antioxidants (RTAs) Trolox and liproxstatin-1 (Fig. 4, C and D, and fig. S19, D to F). As a control, addition of a S_8-preloaded capsule [PC•$(S_8)_2$] did not cause LPO or cell death (Fig. 4C). Conversely, supplementing adipocytes with the S_8 carrier, cucurbit[7]uril/S_8 (CB7•S_8) (*37*), which releases S_8 intracellularly (Fig. 4E and figs. S10, E and F, and S21), protected cells against ferroptosis induced by erastin or RSL3 (Fig. 4F and fig. S19F).

RSL3-induced LPO in mouse adipocytes was suppressed by eNOS overexpression (Fig. 4G and fig. S22A) and enhanced by small interfering RNA (siRNA)–mediated eNOS depletion (fig. S22B). Treatment with buthionine sulfoximine (BSO), an inhibitor of GSH synthesis, decreased S_8 production and increased LPO, potentially owing to depletion of both GSH and its derived sulfur species (including GSSH and GSSSG), as well as S_8 (fig. S23).

To assess the protective role of S_8 against ferroptosis in vivo, we used a mouse osteoarthritis (OA) model (*38*). In both this model and human OA, LPO is detected in the synovium (*39*, *40*) (Fig. 4H), which contains abundant white adipocytes enriched in LDs. We also observed LD-associated S_8 formation in mouse ATDC5 chondrocytes (fig. S24, A and B). We previously reported the therapeutic effect of GSSSG in this OA model (*41*) and found that GSSSG suppresses ferroptosis in cultured chondrocytes (fig. S24C), likely by serving as a substrate for S_8 biosynthesis. Accordingly, injection of CB7•S_8 into the infrapatellar fat pad within the joint cavity immediately after surgery significantly reduced 4-hydroxynonenal (4-HNE) levels, whereas the empty vehicle CB7 had little effect (Fig. 4H and fig. S24D).

To explore how S_8 prevents LPO, we performed the fluorescence-enabled inhibited autoxidation (FENIX) assay (*42*). We prepared artificial LDs (*43*) loaded with S_8, initiated LPO with the lipophilic radical initiator DTUN [(*E*)-1,2-bis((2-methyldecan-2-yl)oxy)diazene] (*42*), and monitored oxidation of the LPO sensor C11-BODIPY. With this FENIX assay, we found that vitamin E, a naturally occurring RTA, delayed LPO (Fig. 5A, left). S_8 alone slowed LPO somewhat, but in combination with GSH, the most abundant intracellular low–molecular weight thiol compound, it markedly and dose-dependently delayed the onset of LPO (Fig. 5A, right). Following the LPO process over time, samples were collected at different time points at start (T_0), during the full inhibition period (T_1), and during LPO periods (T_2 and T_3) (Fig. 5B). Upon incubation of S_8-loaded LDs with GSH, we observed the formation of hydropolysulfides, which were consumed during LPO along with GSH (Fig. 5C and fig. S25). The products of sulfur oxidation GSSG and $HS_2O_3^-$ increased concurrently (fig. S25). This suggests that S_8 in LDs reacts with cellular thiols, such as GSH, to locally generate reactive persulfides that protect LDs from LPO. Thus, S_8 may safeguard LDs against LPO by releasing reactive GSS_nH (Fig. 5D). This hypothesis was further supported by molecular dynamics (MD) simulations. S_8 preferentially localized within the membrane, positioning itself between the head groups and the core of the membrane, and aligned parallel to the acyl chains (Fig. 5E). By contrast, GSH molecules were more stable outside the lipid bilayer or at the interface with the head groups (Fig. 5E). S_8 spontaneously approached the GSH molecules in the head group region, a key prerequisite for the chemical S_8 ring-opening

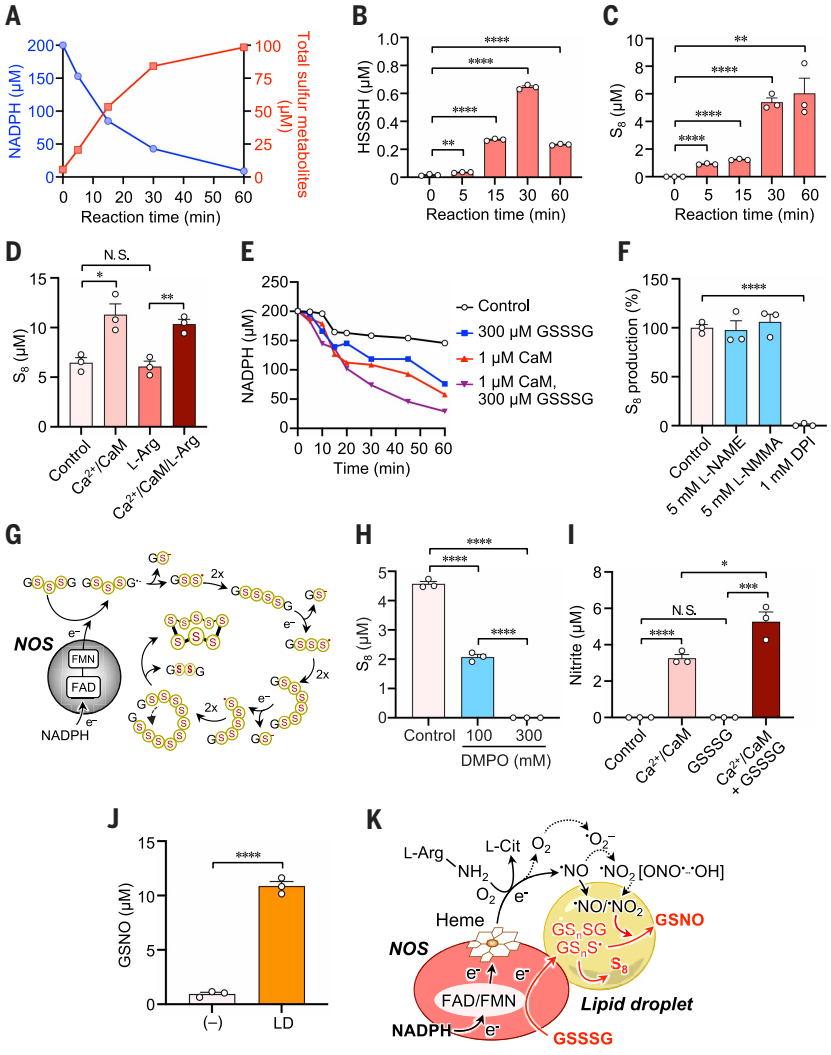

Fig. 3. NOS mediates sulfur chain catenation, leading to S_8 production. (**A**) eNOS-dependent NADPH consumption in the presence of GSSSG and quantification of the sulfur metabolome. Recombinant eNOS (100 nM) was incubated with NADPH (200 μM) and GSSSG (100 μM). NADPH consumption was monitored at 340 nm, and the total sulfur metabolome was calculated from the amounts of sulfur metabolites formed (GSSG, GSSSSG, GSH, GSSH, GSSSH, HSH, HSSH, HSSSH, HSO_3^-, and $HS_2O_3^-$), excluding the substrate GSSSG. (**B**) Time-dependent accumulation of the representative catenated polysulfide HSSSH in reactions containing recombinant eNOS, GSSSG, and NADPH. Conditions were the same as in (A). (**C**) Time-dependent accumulation of S_8 in reactions containing recombinant eNOS, GSSSG, and NADPH. Conditions were the same as in (A). (**D**) Effects of eNOS cofactors Ca^{2+} (1 mM) and CaM (1 μM) and of the substrate L-arginine (3 mM) on eNOS-dependent S_8 production. Conditions were the same as in (A). (**E**) Effects of CaM and GSSSG on eNOS-dependent NADPH consumption in the presence of L-arginine (3 mM). (**F**) Effects of the NOS inhibitors L-NAME (5 mM) and L-NMMA (5 mM), and of the flavin inhibitor DPI (1 mM), on eNOS-dependent S_8 production. Conditions were the same as in(A). (**G**) Proposed mechanism of NOS-dependent sulfur catenation. (**H**) Effect of DMPO on eNOS-dependent S_8 production. Conditions were the same as in (A). (**I**) Effect of GSSSG (300 μM) on eNOS-mediated NO production in the presence or absence of the cofactors Ca^{2+} (1 mM) and CaM (1 μM). NO production was assessed by Griess assay. (**J**) Effect of LDs on GSNO production in reactions containing recombinant eNOS (10 nM), GSSSG (30 μM), L-arginine (300 μM), and NADPH (20 μM). Reactions were performed in the presence or absence of LDs (300 μM TAG). (**K**) Schematic of the proposed cross-talk between sulfur-chain catenation and NO-producing activity of NOS. Higher-order analogs of GSNO (for example, GSSNO) were not detected in this study, consistent with transient formation and rapid conversion to GSNO. The GSNO detected may be interpreted as the net product of a transient pool of GSSNO intermediates. L-Cit, L-citrulline. Data are means ± SD. $^*P < 0.05$, $^{**}P < 0.01$, $^{***}P < 0.001$, $^{****}P < 0.0001$, and N.S. is not significant. Data were analyzed by Student's *t* test (J) or multiple *t* test [(B) to (D), (F), (H), and (I)].

reaction by GSH, ultimately leading to the formation of GSS_nH (Fig. 5F).

Discussion

Elemental sulfur is a key intermediate in the ecological sulfur cycle, in which microorganisms assimilate it from the environment or generate and store it for energy metabolism through oxidation, reduction, or disproportionation. Here, we show that mammalian cells also produce, store, and use S_8. S_8 was detected in mammalian mitochondria and LDs at millimolar concentrations. Although LDs probably acquire S_8 from neighboring mitochondria, LD-associated eNOS provides an additional route for S_8 biogenesis through catenation of glutathione polysulfides, including GSSSG and GSSSSG.

NO and S_8 were independent outputs of eNOS activity. These findings support two distinct but integrated catalytic modes, potentially enabled by electron transfer that prevents competition between NO and S_8 formation (Fig. 3K and fig. S12B). This coupling may also preserve NO bioavailability by limiting eNOS uncoupling. eNOS-dependent S_8 formation suppressed LPO and ferroptosis in adipocytes and HUVECs. In eNOS-CKO mice, loss of adipocyte S_8 increased LPO and oxidative stress, changes that may promote chronic inflammation in adipose tissue (*27*, *44*) (fig. S26). Together, these data identify eNOS-derived S_8 as a physiological defense against LPO-driven oxidative damage and ferroptosis. Consistent with this role, carrier-bound S_8 delivery in vivo can mitigate LPO-driven tissue damage in a mouse model of OA.

Elemental sulfur metabolism may have been retained in modern eukaryotes despite lacking an obvious bioenergetic role. During major evolutionary transitions such as the Archaean temperature drop (*45*) and the Great Oxidation Event (*46*), GSH alone may have been insufficient to prevent LPO and sustain cell survival (*47*). Elemental sulfur, particularly S_8, may therefore have extended the antioxidant capacity of GSH by promoting polysulfide and S_8 formation and thereby strengthening defense against LPO.

Materials and methods

Materials

Recombinant human P450R was purchased from R&D Systems (6340-PRB-020), and XO was purchased from Roche (10110434001). Recombinant NQO1 and FSP1 were prepared as described previously (*48*, *49*). All other chemicals and reagents were obtained from commercial sources, including Nacalai Tesque, FUJIFILM Wako Pure Chemical Industries, Thermo Fisher Scientific (Invitrogen), and Merck (Sigma-Aldrich).

Preparation of PCs

PC, 1-methylpyrene (MP)–encapsulated capsules PC•$(MP)_2$, and the S_8-encapsulated capsules PC•$(S_8)_2$ were prepared according to previous reports (*17*, *50*). An oval-shaped capsule bearing ortho-substituted polyaromatic capsules (oPCs) was likewise synthesized by the reported procedure (*51*). In contrast to the parent meta-substituted capsule PC, ortho substitution on the anthracene capsules enforces a narrower panel angle, leading to a marked contraction of the

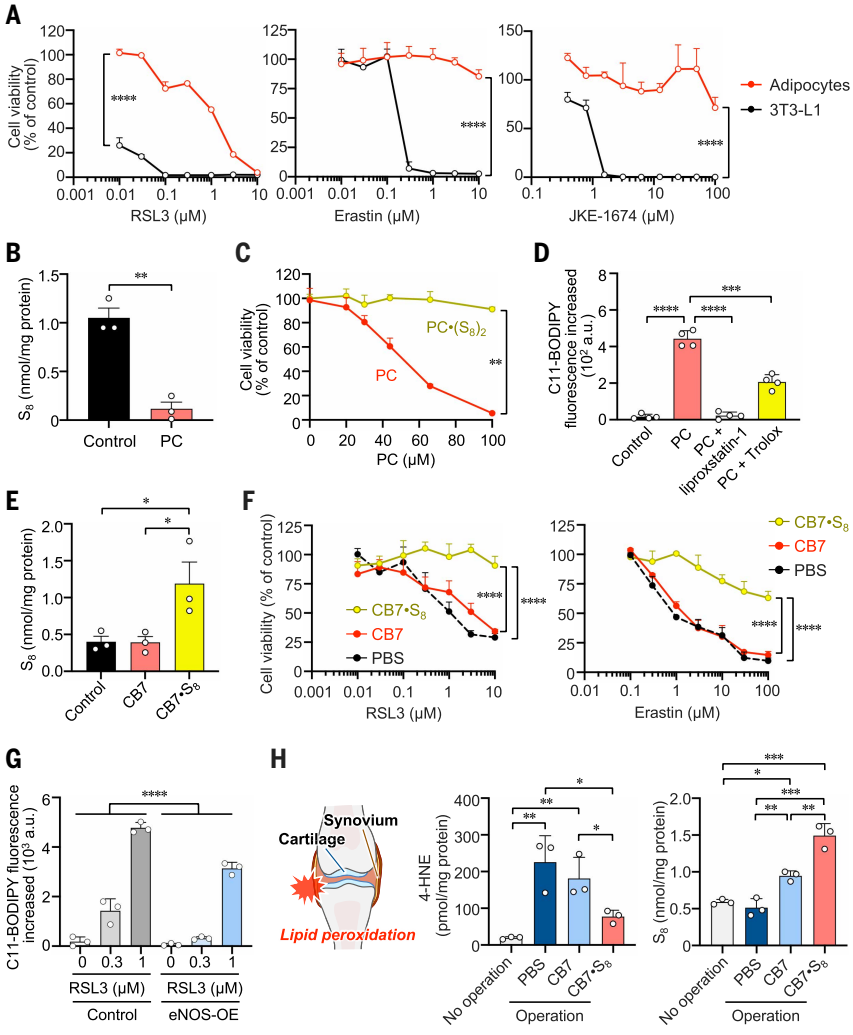

Fig. 4. Protective effects of S_8 on LPO and ferroptosis in 3T3-L1 adipocytes and its role in the OA model. (**A**) Cell viability, assessed by WST-8 assay, in undifferentiated 3T3-L1 cells and differentiated 3T3-L1 adipocytes after 24 hours of exposure to RSL3, erastin, or JKE-1674. (**B**) Quantification of S_8 depletion from 3T3-L1 adipocytes after treatment with PC (50 μM) for 4 hours. Residual free intracellular S_8 was subsequently captured with ortho-substituted PC (oPC) and quantified by MS. (**C**) Cell viability, assessed by WST-8 assay, in 3T3-L1 adipocytes exposed to PC or S_8-loaded PC [PC•$(S_8)_2$] for 4 hours. (**D**) LPO, assessed by C11-BODIPY oxidation, in 3T3-L1 adipocytes treated with PC and antioxidants. Cells were pretreated with liproxstatin-1 (20 μM) or Trolox (200 μM) for 10 min, followed by PC (50 μM) for 1 hour. (**E**) Quantification of S_8 in 3T3-L1 adipocytes treated with CB7 or CB7•S_8 (50 μM) for 1 hour. (**F**) Effect of CB7•S_8 or CB7 on RSL3- or erastin-induced cell death in 3T3-L1 adipocytes. Cells were treated with CB7 or CB7•S_8 (50 μM) for 5 min, followed by RSL3 or erastin for 24 hours, and then subjected to WST-8 assay. (**G**) GPX4-inhibitable LPO, assessed by C11-BODIPY oxidation, in 3T3-L1 adipocytes transfected with control vector or eNOS-OE and exposed to 0, 0.3, or 1 μM RSL3. (**H**) Schematic of the OA model used to induce LPO (4-HNE) in the synovium and cartilage (left). 4-HNE levels in synovium from sham-operated mice or mice analyzed 2 weeks after surgery and treated with phosphate-buffered saline (PBS), CB7, or CB7•S_8 (middle). S_8 levels in synovium from sham-operated mice or mice analyzed 2 weeks after surgery and treated with PBS, CB7, or CB7•S_8 (right). Repeated intra-articular administration of CB7 showed a marginal increase of S_8 (right), potentially owing to prolonged stabilization of S_8 in the chronically inflamed joint cavity. Data are means ± SD. $^*P < 0.05$, $^{**}P < 0.01$, $^{***}P < 0.001$, and $^{****}P < 0.0001$. Data were analyzed by Student's *t* test (B), multiple *t* test [(D) and (H)], one-way ANOVA with Tukey's test (E), or two-way ANOVA with Tukey's test [(A), (C), (F), and (G)].

inner cavity height in oPCs to approximately one-half that of PC. This structural modification was expected to enhance size complementarity toward S_8 and thereby promote tighter host-guest complexation, enabling selective encapsulation of a single S_8 molecule within the cavity.

Preparation of polysulfide derivatives

GSSSG, GSSSSG, cystine trisulfide (CysSSSCys), and other polysulfides used in this study were prepared as previously described (*9*). Amino acid–substituted GSSSG derivatives were synthesized by rhodium-catalyzed sulfur insertion into the corresponding unprotected peptide disulfides, as previously reported (*52*). Stock solutions of GSSSG and its derivatives were prepared at 30 mM in 100 mM HCl and diluted to the indicated concentrations in the assay buffer immediately before use.

Preparation of CB7•S_8 complex

The CB7•S_8 complex was prepared as described previously (*37*). Briefly, CB7 and S_8 were mixed at a 1:1 ratio to give a 10 mM suspension in phosphate-buffered saline (PBS). The suspension was incubated overnight at 37°C with rotary shaking at 1000 rpm and then sterile-filtered through a 0.2-μm filter. The concentration of solubilized S_8 was determined by measuring the absorbance at 263 nm using an extinction coefficient (ε) of 6730 M^{-1} cm^{-1} (*37*).

Bacteria culture

A. vinosum wild-type strain D was cultivated under photosynthetic conditions at 30°C in medium containing 0.12% Na_2S, as described by Bose (*53*). Photosynthetic (anoxic/light) conditions were established by filling screw-capped test tubes with the medium and illuminating them with a light-emitting diode (λ_{max} = 850 nm; CCS, Inc.). *R. capsulatus* wild-type strain SB1003 and the *sqr* mutant described previously (*21*) were cultivated aerobically at 30°C in peptone–yeast extract–starch (PYS) medium (*54*) supplemented with 0.6 mM Na_2S.

Yeast culture

S. pombe strain 972 was used in this study. In *S. pombe*, *hmt2* (heavy metal tolerance 2) encodes a homolog of SQR; therefore, an HMT2-disrupted strain (Δ*hmt2*, hereafter referred to as ΔSQR) was generated using a two-step polymerase chain reaction (PCR) method with minor modifications (*55*). Briefly, 5000–base pair (bp) homologous sequences were added to the kanMX6deletion cassette by two-step overlap PCR using primers and the pFA6-KanMX6 plasmid. The resulting PCR fragment was integrated into the genome by transformation using the LiAc/SS carrier DNA/PEG method (*56*). G418-resistant clones were screened, and correct integration was confirmed by PCR using chromosomal DNA. Yeast cells were cultured in yeast-extract supplemented (YES) medium (0.5% yeast extract, 3% glucose, 0.005% adenine, 0.005% uracil, 0.005% histidine, 0.005% leucine, and 0.005% lysine) starting at an optical density at 600 nm (OD_{600}) of 0.01.

Cell culture

MEFs and HEK293T cells [American Type Culture Collection (ATCC)] were cultured in Dulbecco's Modified Eagle Medium (DMEM; high glucose) supplemented with 10% fetal bovine serum (FBS) and 1% penicillin/streptomycin at 37°C in a humidified atmosphere containing 5% CO_2. ATDC5 cells (RIKEN BRC, Japan), a murine chondrogenic cell line, were cultured in DMEM/Ham's F-12 medium (1:1) supplemented with

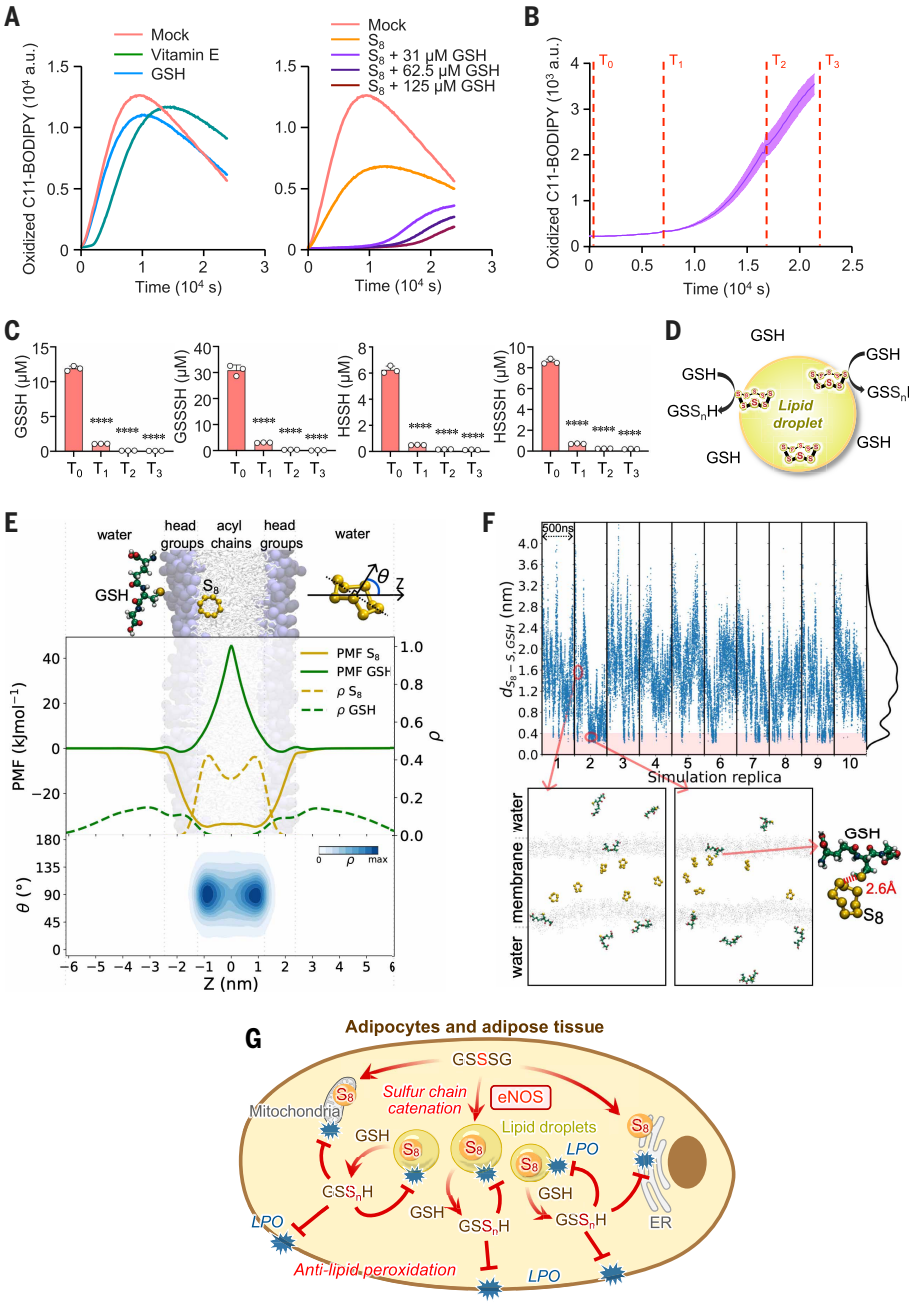

Fig. 5. Mechanism of the protective effect of S_8 against LPO. (**A**) Effects of vitamin E and GSH (left) and of S_8 and S_8 with GSH (right) on LPO, assessed by FENIX assay with C11-BODIPY oxidation, in the artificial LD oxidation system. a.u., arbitrary units. (**B**) Kinetics of LPO in artificial LDs in the presence of S_8 with GSH. T_0 to T_3 indicate the time points at which aliquots were collected for sulfur metabolite analysis. (**C**) Quantification of hydropolysulfides (GSSH, GSSSH, HSSH, and HSSSH) at the indicated time points during LPO in artificial LDs in the presence of S_8 with GSH. (**D**) Proposed mechanism by which S_8 suppresses LPO through release of radical-scavenging GSS_nH species upon reaction with GSH. (**E**) Potential of mean force (PMF) profiles for S_8 and GSH as a function of position along the bilayer normal, *z* (solid lines). Density profiles (ρ) from equilibrium simulations indicate the distributions of each molecule across the bilayer (dashed lines). The bottom heatmap shows the orientation angle, θ, of S_8 relative to the membrane normal (see schematic at top). Snapshots in the top and middle panels show lipid head groups (purple spheres), acyl chains (gray sticks), GSH, and S_8 (sticks). (**F**) Minimum distance ($d_{S8\text{-}S,GSH}$) between sulfur atoms in S_8 and the thiol sulfur of GSH in $n = 10$ independent 500-ns simulation replicas. Distances less than 0.4 nm, which are indicative of intermolecular contact, are highlighted in pink. The normalized distance distribution is shown at the right. Snapshots depict separated S_8 and GSH (left) and a proximal state with a distance of 2.6 Å (right). (**G**) Proposed mechanism by which GSSSG protects against LPO in adipocytes and adipose tissue through S_8 production. GSSSG is reduced by eNOS, promoting sulfur-chain catenation and deposition of S_8 in LDs, thereby suppressing LPO. Data are means ± SD. ****$P < 0.0001$. Data were analyzed by one-way ANOVA with Tukey's test.

5% FBS and 1% penicillin/streptomycin under the same conditions. Confluent 3T3-L1 preadipocytes (ATCC) were induced to differentiate with 10 μg ml^{-1} insulin, 0.5 mM 3-isobutyl-1-methylxanthine, and 1 μM dexamethasone, as described previously (*57*). Two days after induction, cells were maintained in medium containing 10 μg ml^{-1} insulin. HUVECs, human pulmonary artery endothelial cells (HPAECs), human pulmonary microvascular endothelial cells (HPMECs), human coronary artery endothelial cells (HCAECs), human cardiac microvascular endothelial cells (HCMECs), and human aortic endothelial cells (HAoECs) (all from PromoCell, Heidelberg, Germany) were cultured at 37°C in 5% CO_2 using Endothelial Cell Growth Medium (PromoCell), consisting of Endothelial Cell Basal Medium supplemented with 2% fetal calf serum, 0.4% bovine hypothalamic extract, 0.1 ng ml^{-1} recombinant human epidermal growth factor, 1 ng ml^{-1} recombinant human basic fibroblast growth factor, 90 μg ml^{-1} heparin, and 1 μg ml^{-1} hydrocortisone. Cells were passaged at confluence and used within five or six passages. For analysis of intracellular S_8 and sulfur metabolites, cell viability, LPO, and related parameters, cells were treated with the indicated reagents, including A23187, polysulfides, and VEGF, as described in the corresponding figure legends.

Subcellular fractionation

HEK293T cells were harvested and resuspended in 50 mM Tris-HCl and 5 mM ethylenediaminetetraacetic acid (EDTA) (pH 7.4). Cells were homogenized by passage through a 25-gauge needle 30 times. The homogenate was then mixed with 50 mM Tris-HCl, 5 mM EDTA, and 880 mM sucrose (pH 7.4), followed by differential centrifugation at 4°C to isolate subcellular fractions: 1000*g* for 10 min to obtain the nuclear fraction, 8000*g* for 30 min to isolate mitochondria, and 120,000*g* for 1 hour to collect the ER fraction for S_8 quantification.

Isolation of mitochondria from MEFs

MEF mitochondria were isolated by differential centrifugation as described previously, with minor modifications (*22*). MEFs derived from wild-type and mitochondria-specific SQR-deficient mice (*22*) were homogenized in extraction buffer containing 10 mM Tris-HCl, 250 mM sucrose, and 0.5 mM ethylene glycol-bis(β-aminoethyl ether)-*N*,*N*,*N*′,*N*′-tetraacetic acid (pH 7.4) using a glass–Teflon Dounce homogenizer. The homogenate was centrifuged at 2000*g* for 5 min at 4°C to remove nuclei and cell debris. The resulting supernatant was centrifuged at 12,000*g* for 10 min at 4°C, and the mitochondrial pellet was washed three times with buffer and stored at −80°C until use.

Overexpression of eNOS in cells

Transient transfection was performed using Lipofectamine 3000 (Thermo Fisher Scientific) according to the manufacturer's instructions. HEK293T cells were seeded in six-well plates at 1×10^6 cells per well and transfected with 3 μg per well of pPyCAGIP-FLAG-bovine eNOS. Cells were harvested at 24, 48, and 72 hours after transfection and subjected to Western blotting, S_8 quantification, and sulfur metabolome analysis. 3T3-L1 adipocytes differentiated for 4 days were seeded either on 18-mm–by–18-mm coverslips (Matsunami) in 35-mm dishes at 1×10^6 cells per well or in 24-well plates at 5×10^4 cells per well. Cells were transfected with 3 μg per well of pPyCAGIP-FLAG-bovine eNOS, harvested 48 hours later, and subjected to sulfur metabolome analysis, Raman analysis, and LPO measurement.

Knockdown of eNOS in HUVECs

eNOS knockdown was performed as described previously (*10*) using the following siRNAs: negative control (4390843, Ambion) and eNOS-targeting siRNA (4392420, Ambion). HUVECs were seeded in 24-well plates at 5×10^4 cells per well and incubated for 24 hours before transfection. siRNA transfection was performed with Lipofectamine RNAiMAX (Thermo Fisher Scientific) according to the manufacturer's instructions. For each well, 10 pmol siRNA duplex and 1.5 μl Lipofectamine RNAiMAX were each diluted in 100 μl Opti-MEM, combined, and incubated for 20 min at room temperature (RT) before addition to the cells. Cells were incubated for a further 48 hours and then used for Western blotting, S_8 quantification, and LPO measurement.

Mice

Six- to seven-week-old male C57BL/6J mice were purchased from Japan SLC, Inc. Mice were maintained under specific pathogen–free conditions at 24°C and 40% humidity on a controlled light cycle with food and water available ad libitum. All animal experiments were performed in accordance with the Regulations of Animal Experiments and Related Activities at Tohoku University, reviewed by the Institutional Laboratory Animal Care and Use Committee of Tohoku University, and approved by the President of Tohoku University (approval nos. 2019MdA-072-05, 2025MdA-114-01, and 2026MdA-096). Adipocyte-specific eNOS conditional knockout mice were generated by crossing *eNOS*$^{flox/flox}$ mice with Adipoq-iCreERT2 mice. Cre recombination was induced by intraperitoneal injection of tamoxifen (2 mg per mouse per day) for 5 consecutive days starting at 6 weeks of age (*27*). Adipose tissues were collected at 30 weeks of age.

Human breast adipose and omental tissues

Human breast adipose tissue samples were collected from patients undergoing surgery at Tohoku University Graduate School of Medicine. Tumor-side breast adipose tissue was obtained from four female patients with breast cancer (patients 1 to 4; table S1) who underwent mastectomy at Tohoku University Hospital, Sendai, Japan. In addition, three contralateral breast tissue specimens were collected from patient 1 during risk-reducing mastectomy; these tissues were macroscopically free of tumor but carried a *BRCA* mutation. Clinicopathological features are summarized in table S1. Written informed consent was obtained from all participants. The study protocol was approved by the Ethics Committee of Tohoku University School of Medicine (approval no. 2022-1-950). Omental tissue was collected during esophagectomy for gastrointestinal stromal tumor. The right margin of the gastric omentum, outside the primary esophageal resection field, was excised using an ultrasonically activated device. Thermally affected tissue was removed, and the remaining specimen was immediately frozen in liquid nitrogen. According to the surgeon's assessment, the omental tissue was free of pathological involvement. Written informed consent was obtained from the participant, and the protocol was approved by the Ethics Committee of the Graduate School of Medicine (approval no. 2024-1-770).

Isolation of LDs from 3T3-L1 adipocytes and human adipose tissue

3T3-L1 adipocytes were washed twice with ice-cold PBS, scraped into PBS, pooled, and centrifuged at 180*g* for 3 min at RT. Pellets were resuspended in hypotonic Tris-EDTA buffer (10 mM Tris-HCl, 1 mM EDTA, pH 7.4), incubated on ice for 10 min, and homogenized with 10 strokes at 1000 rpm using a glass–Teflon Dounce homogenizer. Human adipose tissue was minced and digested for 60 min at 37°C with shaking in PBS containing 1.5 μg ml^{-1} collagenase D (Sigma-Aldrich), 0.24 μg ml^{-1} Dispase II (Sigma-Aldrich), and 10 mM $CaCl_2$. Undigested tissue was removed through a 250-μm nylon mesh (Thermo Fisher Scientific), and the filtrate was centrifuged at 700*g* for 10 min at RT. Floating adipocytes were collected, resuspended in Tris-EDTA buffer, incubated on ice for 10 min, and homogenized as above. LDs were isolated as described previously (*58*). Lysates were centrifuged at 26,000*g* for 30 min at 4°C, and the floating LD layer was collected and adjusted to 25% sucrose and 100 mM sodium carbonate. Samples were layered over a 60% sucrose cushion, overlaid with 100 mM sodium carbonate and Tris-EDTA buffer, and centrifuged again at 26,000*g* for 30 min at 4°C, and the floating LDs were collected into fresh 1.5-ml tubes and washed three times with ice-cold Tris-EDTA buffer.

Exhaled breath condensate collection

Exhaled breath condensate (EBC) was collected noninvasively using a freezing condenser device connected to a mouthpiece and a 50-ml polystyrene tube, as described previously (*59*). Healthy volunteers [56 ± 3.9 years, mean ± SD; $n = 20$ (11 male and 9 female)] and patients with breast cancer with a clinical history of less than 5 years [57 ± 9.3 years, mean ± SD; $n = 19$ (all female)] breathed through the mouthpiece at normal frequency and tidal volume for 5 to 10 min while seated comfortably, yielding ~0.5 to 1 ml EBC. The mouthpiece was connected to a 50-ml polystyrene tube placed in a Peltier device (GL Sciences), and exhaled breath was condensed by rapid cooling to −20°C. Samples were immediately stored at −80°C until sulfur metabolome analysis. This study was approved by the Ethics Committees of the Tohoku University Graduate School of Medicine (approval no. 2023-1-800) and Tohoku University Graduate School of Dentistry (approval no. 35331). Written informed consent was obtained from all participants.

Expression and purification of recombinant NOS proteins

cDNAs encoding eNOS, neuronal NOS (nNOS) and inducible NOS (iNOS) were cloned into pCW vectors. Recombinant rat nNOS and bovine eNOS were expressed in *Escherichia coli* BL21 cells and purified using 2′,5′-ADP-Sepharose (Sigma-Aldrich) as described previously (*60*). Recombinant rat iNOS was coexpressed with pSTV28-rat CaM in *E. coli* BL21 cells and purified using 2′,5′-ADP-Sepharose (Sigma-Aldrich), similarly using a modified protocol (*61*). Proteins were desalted on PD-10 columns (GE Healthcare) into 50 mM Tris-HCl (pH 7.5) and 0.1 mM EDTA, stored at −80°C, and quantified with Protein Assay Coomassie Brilliant Blue (CBB) Solution (Nacalai Tesque). Purity was assessed by SDS–polyacrylamide gel electrophoresis (PAGE) with CBB staining.

PC-mediated S_8 encapsulation and its chemical analyses

Formation of S_8-encapsulated PCs was analyzed by ^{1}H nuclear magnetic resonance (NMR). PC and PC•$(S_8)_2$ were prepared in D_2O by incubating PC with S_8, followed by centrifugation and filtration to remove insoluble S_8. ^{1}H NMR spectra confirmed formation of PC•$(S_8)_2$, consistent with stable encapsulation of S_8 by PC. Formation of the S_8-encapsulated oPC complex was analyzed similarly. S_8 (0.14 mg, 0.55 μmol, 5.5 equiv.) was added to an aqueous solution of oPC (0.4 mg, 0.1 μmol; 0.5 ml total volume) in a glass tube, and the mixture was stirred at RT for 3 hours. Selective formation of the 1:1 host-guest complex oPC•S_8 was confirmed by NMR and electrospray ionization time-of-flight MS (ESI-TOF MS). The kinetics of S_8 capture by PC

were then examined during transfer of S_8 from CB7•S_8 to PC. ^{1}H NMR spectra (500 MHz, D_2O, RT) were acquired over time after addition of CB7•S_8 to PC. PC (3.6 mg, 0.94 μmol) was dissolved in D_2O (1.7 ml) in a 7-ml test tube and stirred at 80°C for 10 min. After cooling to RT, the solution was filtered through a 200-nm membrane to give a clear, colorless solution. The concentration of PC was estimated as 0.1 mM by UV-visible spectroscopy and confirmed by NMR integration. An aliquot (340 μl) was transferred to an NMR tube and mixed with a D_2O solution of CB7•S_8 (1.0 mM, 260 μl, 7.5 equiv. relative to S_8). The sample was shaken, analyzed immediately by ^{1}H NMR, stored at RT, and reanalyzed periodically. Transfer of S_8 was quantified by integrating signals for PC and S_8-loaded PC•$(S_8)_2$.

Extraction and PC encapsulation of intracellular S_8

S_8 was captured from biological samples by PC encapsulation after Folch extraction. Adherent cells (HEK293T, HUVECs, HPAECs, HPMECs, HCAECs, HCMECs, HAoECs and 3T3-L1 adipocytes) cultured in six-well plates were washed twice with ice-cold 0.9% NaCl, scraped into 55% methanol (MeOH), and transferred to chloroform ($CHCl_3$) to give a final $CHCl_3$/MeOH/H_2O volume of 320:150:120 μl per well. *A. vinosum* and *R. capsulatus* cultures grown to an OD_{660} of 1.5 were harvested from 250-μl aliquots by centrifugation (20,000*g*, 5 min, 4°C), washed with 250 μl PBS, and resuspended in 150 μl H_2O, 170 μl MeOH, and 400 μl $CHCl_3$. Samples were lysed by probe sonication (5 s, 40% intensity, five cycles) and shaken at 500 rpm for 30 min. Yeast from a 5-ml culture (OD_{600} = 4.35) was resuspended in 100 μl PBS, mixed with 200 μl $CHCl_3$ and 100 μl MeOH, and disrupted by probe sonication (10 s, 30% intensity, five cycles). The subcellular fractions from HEK293T cells and mouse brown adipose tissues, white adipose tissues, and synovium were homogenized in 180 μl H_2O and 225 μl MeOH, followed by addition of 480 μl $CHCl_3$ and shaking at 500 rpm for 10 min. Isolated LDs (10 μl) were mixed with 90 μl H_2O, 130 μl MeOH, and 300 μl $CHCl_3$ and then shaken at 500 rpm for 10 min. All samples were vortexed for 30 s and centrifuged at 20,000*g* for 5 min at 4°C to induce phase separation. The lower $CHCl_3$ phase was collected, dried under N_2, and resuspended in MeOH containing PC and the internal standard PC•$(MP)_2$ to a final volume of 50 μl [50 μM PC and 3 μM PC•$(MP)_2$]. After incubation for 30 min at RT, samples were centrifuged again (20,000*g*, 5 min, 4°C), and the supernatants were analyzed by liquid chromatography MS/MS (LC-MS/MS).

Quantitative LC-MS/MS analysis of PC-encapsulated S_8

For quantification of S_8-containing PCs, 2 μl of sample was analyzed on an LCMS-8060NX mass spectrometer coupled to a Nexera UHPLC system (Shimadzu) in flow-injection mode. The mobile phase was 50% MeOH containing 0.1% formic acid at 0.2 ml min^{-1}. Electrospray ionization settings were as follows: nebulizer gas, 2.7 liters min^{-1}; heating gas, 10 liters min^{-1}; drying gas, 6 liters min^{-1}; interface temperature, 200°C; desolvation line temperature, 100°C; heat block temperature, 100°C; and collision-induced dissociation gas pressure, 270 mPa. Multiple reaction monitoring (MRM) transitions were mass/charge ratio (*m*/*z*) 968.8 → 904.1 for PC•S_8, 1032.8 → 904.1 for PC•$(S_8)_2$, and 958.0 → 904.1 for PC•$(MP)_2$. Dwell time was 100 ms, and collision energy was −35 eV. Peak areas were integrated in LabSolutions v5.114 (Shimadzu). A calibration curve generated with PC•$(S_8)_2$ was run in parallel, and S_8 concentrations were calculated from the ratio of S_8-capsule to MP-capsule signal. $CHCl_3$ was used as the blank. For normalization, the remaining upper fraction containing precipitated proteins was lyophilized and dissolved in 0.1% SDS and 0.2 M NaOH for 60 min at 50°C. Protein concentration was measured with a BCA assay kit (Nacalai Tesque), and S_8 levels were converted to intracellular concentrations using cell volume where indicated. Alternatively, total triacylglycerol was quantified with the Triglyceride-Glo Assay (Promega) according to the manufacturer's instructions and used to normalize lipid droplet-associated S_8.

Evaluation of intracellular S_8 depletion by PC treatment

To assess the reduction in intracellular S_8 levels after PC treatment, differentiated 3T3-L1 adipocytes were incubated in culture medium containing 50 μM PC for 4 hours at 37°C under 5% CO_2. After washing, intracellular free S_8 was extracted with $CHCl_3$/MeOH/H_2O as described above. The dried extract was then resuspended in a total volume of 50 μl containing 25 μl MeOH, 50 μM oPC, and 3 μM PC•$(MP)_2$ and incubated for 30 min at RT. The samples were subsequently centrifuged at 20,000*g* for 5 min at 4°C, and the resulting supernatant was subjected to LC-MS/MS analysis of S_8. The MRM transition for S_8-bound oPC (oPC•S_8) was set to *m*/*z* 856.2 → 100.1, with a dwell time of 100 ms and a collision energy of −35 eV. All other LC-MS/MS conditions were as described above. The effects of PC treatment on cells and LDs were also analyzed by Raman spectroscopy, as described in a later section.

Estimation of mitochondrial S_8 concentration

The apparent intramitochondrial S_8 concentration was calculated from the amount of S_8 measured in isolated HEK293T mitochondria, total mitochondrial protein, and estimated mitochondrial volume. Mitochondrial volume was estimated from confocal measurements of mitochondrial diameter, assuming spherical geometry ($V = 4/3\pi r^3$), which yielded an average volume of 0.52 fl per mitochondrion, consistent with values reported from 3D confocal imaging in HEK293 cells and related systems (*62*, *63*). Total mitochondrial volume per sample was estimated by multiplying the average mitochondrial volume by the number of mitochondria per cell and the number of cells used for mitochondrial preparation. The apparent intramitochondrial S_8 concentration was then derived from the measured amount of S_8 per mitochondrial protein, total mitochondrial protein, and total mitochondrial volume.

Triphenylphosphine-based sulfane sulfur measurement

This protocol was adapted from a previously reported method (*64*). Isolated LDs from 3T3-L1 cells (300 μl) were mixed with $CHCl_3$ (300 μl) and MeOH (260 μl), vortexed for 30 s and incubated on a rotary shaker at 1000 rpm for 10 min. Samples were then centrifuged at 20,000*g* at 4°C. The lower $CHCl_3$ phase was transferred to a glass vial and dried under a stream of N_2. The dried fraction was resuspended in toluene (100 μl) containing 100 μM tris(2,4,6-trimethoxyphenyl)phosphine [triphenylphosphine, $(Ph)_3P$; Sigma-Aldrich] and incubated for 1 hour at RT. The reaction mixture was then diluted 1000-fold in MeOH, and the internal standard [$(Ph)_3P{=}^{34}S$; 3 μM], which was synthesized as described previously (*65*), was added. The resulting mixture was analyzed by LC-MS/MS (LCMS-8060, Shimadzu). Chromatographic separation was performed on a YMC-Triart C18 column (50 × 2.0 mm internal diameter, 3 μm) maintained at 40°C, using mobile phase A (0.1% formic acid in water) and mobile phase B (0.1% formic acid in MeOH) at a flow rate of 0.2 ml min^{-1}. The gradient was as follows: 0 to 2 min, 1% B; 2 to 7 min, 1 to 80% B; 7 to 12 min, 80 to 99% B; 12 to 15 min, 99% B; and 15 to 22 min, 99 to 1% B. The autosampler injector was washed for 9 s before and after each injection with $CHCl_3$/acetone (70:30, v/v). The ESI source was operated with a nebulizer gas flow of 3 liters min^{-1}, heating gas flow of 15 liters min^{-1}, drying gas flow of 3 liters min^{-1}, interface temperature of 400°C, desolvation-line temperature of 250°C, and heat-block temperature of 400°C. MRM transitions were set to *m*/*z* 565 → 397 for $(Ph)_3P{=}^{32}S$ and *m*/*z* 567 → 399 for $(Ph)_3P{=}^{34}S$, with a dwell time of 100 ms per transition and a collision energy of −20 eV.

Spike-and-recovery assay for sulfane sulfur in LDs

To assess the extraction and recovery efficiency of sulfane sulfur from LDs by the phosphine method, spike-and-recovery experiments were performed using stable isotope-labeled $^{34}S_8$. For the positive control, corresponding to 100% recovery, a 30-μl aliquot of $CHCl_3$ containing 0.5 μM $^{34}S_8$ was mixed directly with 30 μl of 1 mM $(Ph)_3P$ in toluene.

The mixture was incubated at RT for 1 hour, diluted appropriately, and analyzed by LC-MS/MS. For recovery measurements, a 30-µl aliquot of the isolated LD-containing fraction was spiked with 30 µl of 0.5 µM $^{34}S_8$ in $CHCl_3$ and combined with 26 µl of MeOH. The mixture was vortexed for 30 s, shaken for 10 min, and centrifuged to induce phase separation. A 20-µl aliquot of the lower $CHCl_3$ phase was collected and incubated with 20 µl of 1 mM $(Ph)_3P$ in toluene at RT for 1 hour. The resulting mixture was diluted and analyzed by LC-MS/MS. Recovery efficiency was calculated by comparing the peak areas of recovery samples with those of the corresponding positive controls, yielding a recovery of 61.8 ± 3.8% ($n = 3$, mean ± SD). The endogenous sulfane sulfur (S^0) content in LDs determined by the triphosphine method was subsequently corrected using this recovery factor.

Raman imaging of S_8 in LDs and cells

Raman spectroscopy was performed on a LabRAM HR Evolution microscope (HORIBA) equipped with a 785-nm laser to minimize fluorescence background and improve resolution in the sulfur-derived low–wave number region. Laser power was set to 100 mW to avoid thermal degradation. Raman signals were collected in backscattering mode through a 100× objective. Spectra were acquired over 0 to 2400 cm^{-1} with integration times of 30 s for S_8 in glyceryl trioleate (triolein), 60 s for isolated LDs, and 120 s for cells. For Raman imaging, a 100-µm–by–100-µm area was mapped at 1-µm intervals with an integration time of 120 s per point. For preparation of the S_8 standard in triolein, 8 mg of S_8 powder was dissolved in 1 ml triolein, and the supernatant containing S_8-encapsulated lipid vesicles was used for analysis. Raman analysis was used to determine whether PC or oPC captures S_8 in isolated and intracellular LDs from HUVECs and adipocytes. S_8 was quantified in isolated LDs incubated with 0.2 µM eNOS, 2 mM GSSSG, and 2 mM NADPH in the absence or presence of 100 µM PC or oPC. Endogenous S_8 capture by PC was also examined in LDs from adipocytes and HUVECs. Cells were incubated with 50 µM oleic acid (HUVECs only) and 2 mM CysSH for 24 hours, followed by 1 mM GSSSG for 2 hours and 20 µM A23187 for 10 min, washed, and then treated with or without 50 µM PC for 30 min. To analyze CB7•S_8-mediated delivery of S_8 to LDs in HUVECs, cells were incubated with 50 µM oleic acid for 24 hours, washed, and then treated with 300 µM CB7 or CB7•S_8 for 3 hours. CB7•S_8-mediated S_8 delivery was analyzed similarly in 3T3-L1 adipocytes after treatment with 500 µM CB7 or CB7•S_8 for 3 hours. Cells seeded on micro cover glass (18 mm by 18 mm) were treated with GSSSG, PC, oPC, CB7, or CB7•S_8 and mounted on micro-slide glass (76 mm by 26 mm, Matsunami) for analysis. Isolated LDs treated with reagents were spread onto microslide glass, covered with microcover, glass and analyzed. Data were analyzed using LabSpec 6 software (HORIBA FRANCE SAS). S_8 signals in LDs were normalized to the lipid peak at 1444 cm^{-1}, and Raman maps were generated from the integrated intensity of sulfur peaks.

Sulfur metabolomics by HPE-IAM and LC-MS/MS

Sulfur metabolome analysis of recombinant proteins, cells, and artificial LDs was performed as described previously (*10*, *59*, *66*). Enzyme reaction mixtures, cell cultures (HEK293T cells, HUVECs and 3T3-L1 adipocytes), EBC, and S_8-containing artificial LDs were incubated with 5 mM β-(4-hydroxyphenyl)ethyl iodoacetamide (HPE-IAM) in MeOH and 20 mM sodium acetate buffer (pH 6.5) for 20 min at 37°C. After centrifugation at 14,000*g* for 10 min at 4°C, the supernatants were diluted with 0.1% formic acid containing known amounts of isotope-labeled internal standards and analyzed by LC-MS/MS on an LCMS-8060NX system (Shimadzu). LC-MS/MS parameters and synthesis of the isotope-labeled internal standards were performed as reported previously (*10*, *59*, *66*).

Proteome analysis of LDs

Delipidation of LDs isolated from 3T3-L1 adipocytes was performed with minor modifications to a previously described method (*58*). Briefly, 100 µl of the LD fraction was incubated with 1 ml cold acetone overnight at −30°C and then centrifuged at 14,000*g* and 4°C for 30 min. After the solvent was removed, the protein pellet was sequentially extracted with acetone at RT, 1:1 acetone:ether (v/v), and ether. Residual solvent was evaporated under nitrogen, and the resulting pellet was used for proteome analysis. The pellet was dissolved in 50 mM ammonium bicarbonate containing 0.05% ProteaseMAX Surfactant (Promega), reduced with 5 mM dithiothreitol at 56°C for 20 min, and alkylated with 15 mM IAM at 25°C for 15 min. Proteins were digested with 20 ng ml^{-1} Trypsin Gold at 37°C for 3 hours and analyzed by liquid chromatography–electrospray ionization–quadrupole time-of-flight tandem MS (LC-ESI-Q-TOF MS/MS) using a 6545XT AdvanceBio LC/Q-TOF system (Agilent Technologies). Proteins were identified with Agilent MassHunter BioConfirm software (version 10.0).

Biochemistry of NOS-mediated S_8 biosynthesis

Standard assays were performed at 37°C in 20 µl containing 40 mM Tris-HCl (pH 7.6), 0.2 mM NADPH, and 0.1 µM NOS, with or without 1 mM $CaCl_2$, 1 µM CaM, 3 mM L-arginine, and 100 to 300 µM GSSSG. Reactions were started by NADPH addition. Similar conditions were used for P450R, NQO1, XO, and FSP1; menadione, xanthine, and coenzyme Q1 were used as substrates for NQO1, XO, and FSP1, respectively. Various GSSSG derivatives were tested as NOS substrates. Sulfur metabolome analysis was performed as described previously (*10*), and in the LC-MS/MS analysis section. NADPH oxidation was monitored at 340 nm at 37°C using an extinction coefficient of 6,220 M^{-1} cm^{-1}. For S_8 analysis, NOS was incubated with GSSSG, NADPH, and 30 µM PC. Samples were diluted with 0.1% formic acid, supplemented with 3 µM PC•$(MP)_2$, and analyzed by LC-MS/MS. For NO analysis, assays were performed at 37°C in 100 µl containing 40 mM Tris-HCl (pH 7.6), 0.2 mM NADPH, 1 mM $CaCl_2$, 10 µM BH_4, 4 µM FAD, 4 µM FMN, 3 mM L-arginine, and 0.1 µM NOS, with or without 1 µM CaM and 300 µM GSSSG. Reactions were started by NADPH addition. NO production was quantified as nitrite by the Griess assay. Samples were incubated with an equal volume of 1% sulfanilamide/4.25% H_3PO_4 for 5 min at RT, followed by *N*-(1-naphthyl)-ethylenediamine dihydrochloride for 10 min, and absorbance at 540 nm was measured with a microplate reader. For GSNO analysis, modified assays were performed at 37°C in 20 µl containing 40 mM Tris-HCl (pH 7.6), 20 µM NADPH, 100 µM $CaCl_2$, 0.1 µM CaM, 1 µM BH_4, 0.4 µM FAD, 0.4 µM FMN, 0.3 mM L-arginine, 30 µM GSSSG, and 10 nM NOS. Reactions proceeded for 30 min in the presence or absence of LDs containing 300 µM TAG. GSNO[^{15}N] (10 µM) was added as an isotope-labeled internal standard. Supernatants were diluted with 0.1% formic acid and analyzed by LC-MS/MS. MRM transitions were m/z 336.7 → 307.2 for GSNO and m/z 337.7 → 307.2 for GSNO[^{15}N], with 32 ms per transition and a collision energy of −11 eV.

Real-time PCR analysis of eNOS and inflammatory genes

Total RNA was extracted from 3T3-L1 adipocytes and epididymal white adipose tissue from wild-type and adipocyte-specific eNOS-CKO mice using TRIzol reagent (Invitrogen). Quantitative real-time PCR (RT-PCR) was performed with a One Step TB Green RT–PCR kit (TaKaRa) on a CFX Connect Real-Time PCR Detection System (Bio-Rad Laboratories) using gene-specific primers. Primer sequences are listed in table S2. Gene expression was normalized to glyceraldehyde-3-phosphate dehydrogenase (GAPDH).

Western blotting

Samples were heat-denatured, resolved by SDS-PAGE, and transferred to polyvinylidene difluoride membranes (Merck Millipore). Membranes were blocked with Blocking One (Nacalai Tesque) and incubated with primary antibodies in TTBS containing 10% Blocking One overnight at 4°C. Primary antibodies were as follows: anti-eNOS (1:500; sc-376751, Santa Cruz Biotechnology), anti-PDI (1:1000; ADI-SPA-891-F, ENZO

Life Sciences), anti-TOM20 (1:1000; ab56783, Abcam), anti-GAPDH (1:1000; M171-3, MBL), anti-FLAG-tag (1:5000; M185-3L, MBL Life Science), and anti-β-actin (1:5000; sc-1615, Santa Cruz Biotechnology). After incubation with appropriate horseradish peroxidase–conjugated secondary antibodies, signals were detected using ECL Prime Western Blotting Detection Reagent and an ImageQuant LAS 500 imager (GE Healthcare).

Fluorescence imaging of LDs, mitochondria, and eNOS

LD staining was performed with minor modifications to a previously described method (*67*). Cells were fixed with 4% paraformaldehyde for 15 min at RT, permeabilized with 0.5% Triton X-100 for 10 min, and stained with 3 μM BODIPY Green (BODIPY 493/503; Thermo Fisher Scientific, D3922) for 15 min. Cells were counterstained with 4′,6-diamidino-2-phenylindole (DAPI), mounted with ProLong Gold Antifade Reagent (Thermo Fisher Scientific, P36982), and imaged on a Nikon C2 plus confocal microscope with NIS Elements version 5.01 software. Mitochondria in live cells were stained according to the manufacturer's instructions as described previously (*10*). HUVECs and ATDC5 cells were seeded in poly-D-lysine–coated eight-well glass chamber slides (Sigma-Aldrich), washed once with PBS, and incubated with 5 μM BODIPY Green and 100 nM MitoTracker Red CMXRos (Thermo Fisher Scientific, M7512) in PBS for 15 min at RT. Excess probe was removed by two washes with PBS before confocal imaging. For eNOS immunocytochemistry, HUVECs treated with or without 20 μM A23187 were analyzed with minor modifications to a previously described method (*10*). Cells were fixed with 4% paraformaldehyde for 15 min at RT, permeabilized with 0.5% Triton X-100 for 10 min, and blocked with 5% goat serum (Jackson ImmunoResearch) for 30 min at 37°C. Cells were incubated with anti-eNOS antibody (1:100) in PBS containing 5% goat serum for 30 min at 37°C, followed by Alexa Fluor 555 goat anti-mouse immunoglobulin G (IgG) (H+L) (A21423, Thermo Fisher Scientific) for 30 min at 37°C. Cells were then stained with 3 μM BODIPY Green and DAPI, mounted with ProLong Gold Antifade Reagent, and imaged by confocal microscopy.

Cell viability

Cell viability was measured with Cell Counting Kit-8 (Dojindo Laboratories) as described previously (*68*). 3T3-L1 cells were seeded in clear 96-well plates at 1×10^4 cells per well in 0.1 ml of medium and differentiated as described above. On day 4 after induction of differentiation, adipocytes were treated with the indicated reagents for 24 hours, washed with PBS, and incubated with 100 μl of phenol red-free DMEM containing 10% WST-8 solution for 2 hours at 37°C. Absorbance at 450 nm was measured with a microplate reader. Cytotoxicity was assessed in parallel by lactate dehydrogenase release using CytoTox-ONE (Promega) according to the manufacturer's instructions. Adipocytes on day 4 of differentiation were treated with the indicated reagents for 24 hours, incubated with CytoTox-ONE reagent for 10 min at 22°C, and then mixed with Stop Solution. Fluorescence was measured with a microplate reader at 560 nm excitation and 590 nm emission.

LPO measurement with C11-BODIPY

LPO was assessed by oxidation of C11-BODIPY (Thermo Fisher Scientific) as described previously (*13*). For confocal imaging, 3T3-L1 adipocytes and ATDC5 cells were seeded in polyethylene imine–coated eight-well glass chamber slides (Sigma-Aldrich) and differentiated as described above. Adipocytes were treated with RSL3, liproxstatin-1, PC, CB7, or CB7•S_8 in DMEM containing 10% FBS and 10 μM C11-BODIPY for 3 hours at 37°C. ATDC5 cells were pretreated with GSSSG at the indicated concentrations for 1 hour and then treated with RSL3 in the presence of 10 μM C11-BODIPY for 3 hours at 37°C. Cells were washed twice with PBS and imaged on a Nikon C2 plus confocal microscope using NIS Elements version 5.01 software with excitation at 561 nm. For flow cytometric analysis, 3T3-L1 adipocytes differentiated for 4 days were seeded in 24-well plates in DMEM containing 10% FBS and treated with RSL3 in the presence of 10 μM C11-BODIPY for 3 hours at 37°C. HUVECs were seeded in 24-well plates in endothelial cell growth medium, treated with RSL3 for 2 hours at 37°C, and then incubated with 10 μM C11-BODIPY for 3 hours at 37°C. Cells were washed with Hank's balanced salt solution (HBSS), detached with TrypLE (Gibco), centrifuged, and resuspended in HBSS. Fluorescence intensity was measured in live cells on a CytoFLEX LX flow cytometer (BECKMAN COULTER) with excitation at 488 nm and emission at 520 nm. Data were analyzed with CytoExpert software (version 2.4). GPX4-inhibitable LPO was defined as the increase in fluorescence induced by RSL3.

Synthesis of S_8-containing artificial LDs

TG 18:1/18:1/18:1 (7.5 μmol; Nu-Chek Prep, T-235) and phosphatidylcholine (1 μmol; Avanti Polar Lipids, 840051) were each dissolved in 100 μl $CHCl_3$/MeOH (3:1, v/v) and combined. Sulfur (S_8, 15.4 mg; Sigma-Aldrich, 213292) was dissolved in 1 ml of $CHCl_3$, and 42 μl was added to the lipid mixture to yield a TG:S_8:phosphatidylcholine ratio of 7.5:2.5:1. The mixture was dried in vacuo in glass vials (Eppendorf Vacufuge 5301). Dried lipids were resuspended in 1.25 ml of ethanol by vortexing for 60 s, followed by bath sonication for 3 min at RT and incubation for 5 min at 37°C in a water bath. Complete dissolution was confirmed by the absence of visible precipitate. To generate artificial LDs, 1.25 ml of the ethanolic lipid suspension was added dropwise to 3.75 ml of PBS containing 0.2% Tween-20 (Sigma-Aldrich, P7949) with stirring, as described previously (*69*). The mixture was stirred for 4 hours at RT in an open container to allow ethanol evaporation, yielding a final lipid concentration of 0.7 mM S_8 per lipid.

FENIX assay for S_8 in LDs

The effect of S_8 in LDs on LPO was examined by FENIX assay as described previously (*42*, *43*). Artificial LDs prepared were appropriately diluted and mixed with C11-BODIPY at artificial LD:C11-BODIPY = 1000:1. A 40-μl aliquot of the artificial LD/C11-BODIPY mixture was added to each well of a 96-well plate, followed by 60 μl of GSH solution (Cayman Chemical) in PBS to give final concentrations of 0.75 mM TAG, 0.25 mM S_8, 1 μM C11-BODIPY, and the indicated GSH concentration. In some FENIX assay, GSH and vitamin E were added in the absence of S_8 at final concentrations of 31 and 0.5 μM, respectively. DTUN [(*E*)-1,2-bis((2-methyldecan-2-yl)oxy) diazene, Cayman Chemical] was dissolved in ethanol as a 13.5 mM stock, and 1.5 μl was added to each 100-μl reaction. Vitamin E served as a reference RTA. A TECAN Spark plate reader was preheated to 37°C, and plates were shaken for 60 s in orbital mode at amplitude 5. Oxidized C11-BODIPY fluorescence was measured with excitation at 488/5 nm and emission at 520/10 nm using a monochromator at a gain of 120. C11-BODIPY stock solutions were prepared in ethanol and stored at −80°C until use.

OA model

OA was induced in 8-week-old male mice by destabilization of the medial meniscus as described previously (*38*). Under general anesthesia and a surgical microscope, the meniscotibial ligament was transected without damaging the medial meniscus. Sham surgery was performed on the contralateral knee without ligament transection. For intra-articular administration, PBS, CB7, and CB7•S_8 were sterile-filtered and injected into the joint cavity to target the infrapatellar fat pad. Immediately after surgery, mice were reanesthetized and given 10 μl PBS, 10 mM CB7, or 800 μM S_8 in 10 mM CB7. In the 2-week treatment group, a second injection was given 1 week later. Mice were euthanized 1 or 2 weeks after surgery, and the infrapatellar fat pad with synovial membrane was collected for S_8 and 4-HNE measurement. Repeated intra-articular administration of the vehicle CB7 may exert a slight

inhibitory effect on 4-HNE production, potentially owing to prolonged stabilization of S_8 in the chronically inflamed joint cavity.

4-HNE measurement in synovial samples

Synovial samples from the mouse OA model were collected 1 and 2 weeks after surgery for 4-HNE measurement. Samples were processed for LC-MS/MS as for S_8 analysis in mouse tissue. Synovial tissue was homogenized in $CHCl_3$/MeOH, centrifuged at 20,000*g* for 5 min at RT, and a 200-µl aliquot of the $CHCl_3$ phase was dried under nitrogen. 4-HNE was derivatized and quantified with minor modifications to a previously described method (*70*). Dried samples were reacted with 2.5 mM 2,4-dinitrophenylhydrazine (DNPH) containing 1 µM 4-HNE-d_3 at 60°C for 2 hours, centrifuged at 20,000*g* for 5 min, diluted threefold with water and analyzed by LC-MS/MS in MRM mode. For protein normalization, an aliquot of the homogenate was dried, incubated with 20 µl of 0.2 M NaOH/0.1% SDS at 60°C for 1 hour, and subjected to BCA assay. 4-HNE values were normalized to protein content. A 10-µl aliquot was injected into an LCMS-8060NX system. Metabolites were separated on a Triart C18 column (50 mm by 2 mm, YMC) with Nexera UHPLC at 40°C and 0.3 ml min^{-1} using mobile phase A (0.1% formic acid) and mobile phase B (0.1% formic acid in MeOH) with a 30 to 100% B gradient from 0 to 13 min and 100% B from 13 to 15 min. Source temperatures were 400°C for the ESI probe, 150°C for the desolvation line, and 400°C for the heat block; nebulizer, heating, and drying gas flows were 3, 10, and 10 liters min^{-1}, respectively. 4-HNE was quantified by isotope-dilution MRM using the transitions m/z 335.0 → 167.0 for the 4-HNE-DNPH adduct and m/z 338.0 → 167.0 for the 4-HNE-d_3-DNPH adduct, with a dwell time of 100 ms and collision energy of 16 eV.

Density functional theory calculations

Density functional theory (DFT) calculations were performed with Gaussian 16 (Rev. C.01) (*71*) on an LX 2U-Twin2 server 406Rh-2 (NEC, Japan) at the Research Center for Computational Science, Japan. Calculations were carried out at the B3LYP/6-31+G(d) level. Optimized structures were confirmed to have no imaginary frequencies. A scaling factor of 1.04 was applied to all calculated frequencies. Calculated Raman intensities were corrected for comparison with experimental measurements (*72*). The Raman spectrum of S_8 powder was measured with a homemade Raman microscope using 785-nm excitation.

MD simulations

MD simulations were performed with Gromacs 2021 (*73*). Lipids were described with CHARMM36 (*74*), water with CHARMM-TIP3P (*75*, *76*), and ions with standard CHARMM parameters (*77*). POPC bilayers were built with CHARMM-GUI Membrane Builder (*78*, *79*) as in our previous study (*80*). Each bilayer contained 162 POPC molecules distributed symmetrically between leaflets and was hydrated with 70 TIP3P water molecules per lipid and 0.15 mM NaCl. Force field parameters for the S_8 and GSH molecules were generated using the CHARMM-GUI Ligand Reader and Modeler tool (https://www.charmm-gui.org/) with the CHARMM36 general force field (CGenFF) (*81*–*83*). S_8 parameters were further refined with Grappa (*84*).

Equilibrium MD simulations

Three explicitly solvated POPC bilayer systems were simulated containing S_8, GSH, or both. System 1 contained one, three, or six S_8 molecules placed randomly in the aqueous phase. System 2 contained six or 10 GSH molecules placed randomly in the aqueous phase. System 3 contained six S_8 molecules in the bilayer and either six or 10 GSH molecules in the aqueous phase to examine S_8-GSH interactions. Molecules were inserted with gmx insert-molecules. After insertion, systems were energy-minimized by steepest descent until the maximum force was less than 1000 kJ mol^{-1} nm^{-1}. Bonds involving hydrogen were constrained with LINCS (*85*), and water geometry with SETTLE (*86*). Neighbor searching used the Verlet scheme (*87*) with updates every 20 steps. Long-range electrostatics were treated with PME (*88*, *89*) and short-range Lennard-Jones interactions with a 1.0-nm cutoff. Systems were thermalized in the NVT ensemble at 298 K using the Nosé-Hoover thermostat (*90*, *91*) (τ_T = 1.0 ps). Equilibration and production were performed in the NPT ensemble with separate temperature coupling for membrane and solvent. Pressure was controlled with the Berendsen barostat (*92*) during equilibration and the semisotropic Parrinello-Rahman barostat (*93*) during production (τ_P = 5.0 ps; compressibility, 4.5×10^{-5} bar^{-1}). Equations of motion were integrated with the leapfrog algorithm using a 2-fs timestep. For S_8-only systems, six 300-ns replicas were run for each S_8 copy number (one, three, or six). For GSH-only systems, six 400-ns replicas were run for each GSH copy number (six or 10). For combined S_8/GSH systems, five 500-ns replicas were run for each GSH copy number (six or 10). Solute positions along the membrane normal (z) were monitored throughout. The density profiles in Fig. 5E show normalized z distributions for system 1 and system 2. S_8 orientation was quantified as the angle between the ring normal and the membrane normal and plotted as a function of $z(\theta)$ in Fig. 5E using system 1 trajectories. The first half of each replica was discarded for these analyses. In system 3, the distance between any sulfur atom of S_8 and the sulfur atom of GSH ($d_{S8\text{-}S,GSH}$) was extracted. Time traces for the 10 combined-system replicas and the normalized distance distribution are shown in Fig. 5F. Snapshots were rendered with VMD (*94*), and statistical analyses were performed with MDAnalysis (*95*, *96*).

Umbrella sampling MD simulations

Potentials of mean force (PMFs) for S_8 and GSH across the bilayer were calculated by umbrella sampling as described by Diedrich *et al.* (*80*) and established protocols (*97*). A harmonic umbrella potential of 1000 kJ mol^{-1} nm^{-2} was applied along z with windows spaced 0.025 nm apart. To improve sampling, molecules were arranged in two columns spanning positions inside and outside the bilayer with a 1.5-nm offset and 3.64-nm lateral separation. A flat-bottom harmonic potential was applied along y to prevent interactions between columns (*97*). Overlaps among solutes, lipids and water were resolved by gradually turning on Lennard-Jones and electrostatic interactions over 10 ps of Langevin stochastic dynamics using the Gromacs free-energy routine; a dummy atom was placed at the center of the S_8 ring to prevent acyl-chain penetration. Systems were then energy-minimized and equilibrated by 25 ps NVT at 298 K with the Nosé-Hoover thermostat and 2 ns NPT at 1 bar with the Berendsen barostat. During preparation, position restraints were applied to solute atoms and lipid phosphorus atoms, together with dihedral restraints at the lipid headgroup–tail interface. Umbrella production simulations were run for 50 ns per window for S_8 and 100 ns per window for GSH, after removal of dummy atoms and restraints. PMFs were calculated by WHAM (*98*) using gmx wham (*99*). Uncertainty was estimated by bootstrapping (*99*) and did not exceed 0.68 kJ mol^{-1}. Convergence was assessed by backward block averaging after excluding the first half of each window, and PMFs were symmetrized about the bilayer center. The PMF showed a quasi-uniform well for S_8 within the acyl-chain region of the bilayer with a depth of −34.86 kJ mol^{-1} relative to water, indicating favorable partitioning into the hydrophobic core. By contrast, GSH showed an energy barrier of 45.39 kJ mol^{-1} at the bilayer center. A metastable region permissive for the S_8-GSH interaction was predicted near the acyl-chain headgroup interface.

Statistics and reproducibility

Data are means ± SD of at least three independent experiments unless otherwise specified. The n number is defined as biological independent samples or animals unless otherwise specified. The n numbers in all experiments are described in the legends or Materials and methods. P values less than 0.05 were said to be significant. We used GraphPad Prism 9 (GraphPad Software) for statistical analysis.

REFERENCES AND NOTES

1. W. Martin, J. Baross, D. Kelley, M. J. Russell, Hydrothermal vents and the origin of life. *Nat. Rev. Microbiol.* **6**, 805–814 (2008). doi: 10.1038/nrmicro1991; pmid: 18820700
2. M. S. Dodd *et al.*, Evidence for early life in Earth's oldest hydrothermal vent precipitates. *Nature* **543**, 60–64 (2017). doi: 10.1038/nature21377; pmid: 28252057
3. K. Mateos *et al.*, The evolution and spread of sulfur cycling enzymes reflect the redox state of the early Earth. *Sci. Adv.* **9**, eade4847 (2023). doi: 10.1126/sciadv.ade4847; pmid: 37418533
4. H. van Gemerden, Microbial mats: A joint venture. *Mar. Geol.* **113**, 3–25 (1993). doi: 10.1016/0025-3227(93)90146-M
5. R. Hedderich *et al.*, Anaerobic respiration with elemental sulfur and with disulfides. *FEMS Microbiol. Rev.* **22**, 353–381 (1998). doi: 10.1111/j.1574-6976.1998.tb00376.x
6. Z. Zhou, P. Q. Tran, E. S. Cowley, E. Trembath-Reichert, K. Anantharaman, Diversity and ecology of microbial sulfur metabolism. *Nat. Rev. Microbiol.* **23**, 122–140 (2025). doi: 10.1038/s41579-024-01104-3; pmid: 39420098
7. R. M. Cooper, J. S. Williams, Elemental sulphur as an induced antifungal substance in plant defence. *J. Exp. Bot.* **55**, 1947–1953 (2004). doi: 10.1093/jxb/erh179; pmid: 15181110
8. D. G. Searcy, Elemental sulfur reduction to H_2S by *Tetrahymena thermophila*. *Eur. J. Protistol.* **62**, 56–68 (2018). doi: 10.1016/j.ejop.2017.11.004; pmid: 29248819
9. T. Ida *et al.*, Reactive cysteine persulfides and S-polythiolation regulate oxidative stress and redox signaling. *Proc. Natl. Acad. Sci. U.S.A.* **111**, 7606–7611 (2014). doi: 10.1073/pnas.1321232111; pmid: 24733942
10. T. Akaike *et al.*, Cysteinyl-tRNA synthetase governs cysteine polysulfidation and mitochondrial bioenergetics. *Nat. Commun.* **8**, 1177 (2017). doi: 10.1038/s41467-017-01311-y; pmid: 29079736
11. R. Greiner *et al.*, Polysulfides link H_2S to protein thiol oxidation. *Antioxid. Redox Signal.* **19**, 1749–1765 (2013). doi: 10.1089/ars.2012.5041; pmid: 23646934
12. N. Sen *et al.*, Hydrogen sulfide-linked sulfhydration of NF-κB mediates its antiapoptotic actions. *Mol. Cell* **45**, 13–24 (2012). doi: 10.1016/j.molcel.2011.10.021; pmid: 22244329
13. U. Barayeu *et al.*, Hydropersulfides inhibit lipid peroxidation and ferroptosis by scavenging radicals. *Nat. Chem. Biol.* **19**, 28–37 (2023). doi: 10.1038/s41589-022-01145-w; pmid: 36109647
14. Z. Wu *et al.*, Hydropersulfides inhibit lipid peroxidation and protect cells from ferroptosis. *J. Am. Chem. Soc.* **144**, 15825–15837 (2022). doi: 10.1021/jacs.2c06804; pmid: 35977425
15. Z. Wu, U. Barayeu, D. Schilling, T. P. Dick, D. A. Pratt, Emergence of (hydro)persulfides as suppressors of lipid peroxidation and ferroptotic cell death. *Curr. Opin. Chem. Biol.* **76**, 102353 (2023). doi: 10.1016/j.cbpa.2023.102353; pmid: 37356334
16. F.-C. A. Kafantaris, G. K. Druschel, Kinetics of the nucleophilic dissolution of hydrophobic and hydrophilic elemental sulfur sols by sulfide. *Geochim. Cosmochim. Acta* **269**, 554–565 (2020). doi: 10.1016/j.gca.2019.11.010
17. S. Matsuno *et al.*, Exact mass analysis of sulfur clusters upon encapsulation by a polyaromatic capsular matrix. *Nat. Commun.* **8**, 749 (2017). doi: 10.1038/s41467-017-00605-5; pmid: 28963533
18. M. Yoshizawa, L. Catti, Bent anthracene dimers as versatile building blocks for supramolecular capsules. *Acc. Chem. Res.* **52**, 2392–2404 (2019). doi: 10.1021/acs.accounts.9b00301; pmid: 31347840
19. Z. Wang, M. Wu, An integrated phylogenomic approach toward pinpointing the origin of mitochondria. *Sci. Rep.* **5**, 7949 (2015). doi: 10.1038/srep07949; pmid: 25609566
20. N.-U. Frigaard, C. Dahl, "Sulfur metabolism in phototrophic sulfur bacteria" in *Advances in Microbial Physiology*, **vol. 54**, R. K. Poole, Ed. (Academic Press, 2008), pp. 103–200.
21. T. Shimizu *et al.*, Polysulfide metabolizing enzymes influence SqrR-mediated sulfide-induced transcription by impacting intracellular polysulfide dynamics. *PNAS Nexus* **2**, pgad048 (2023). pmid: 36909821
22. E. Marutani *et al.*, Sulfide catabolism ameliorates hypoxic brain injury. *Nat. Commun.* **12**, 3108 (2021). doi: 10.1038/s41467-021-23363-x; pmid: 34035265
23. P. D. Bartlett, G. Meguerian, Reactions of elemental sulfur. I. The uncatalyzed reaction of sulfur with triarylphosphines1. *J. Am. Chem. Soc.* **78**, 3710–3715 (1956). doi: 10.1021/ja01596a043
24. A. Rensonnet *et al.*, Spectral fingerprinting of cellular lipid droplets using stimulated Raman scattering microscopy and chemometric analysis. *Analyst* **149**, 553–562 (2024). doi: 10.1039/D3AN01684F; pmid: 38088863
25. V. Vitvitsky *et al.*, Structural and mechanistic insights into hemoglobin-catalyzed hydrogen sulfide oxidation and the fate of polysulfide products. *J. Biol. Chem.* **292**, 5584–5592 (2017). doi: 10.1074/jbc.M117.774943; pmid: 28213526
26. Y. Yamada *et al.*, Suppressive role of PPARγ-regulated endothelial nitric oxide synthase in adipocyte lipolysis. *PLOS ONE* **10**, e0136597 (2015). doi: 10.1371/journal.pone.0136597; pmid: 26317347
27. A. W. C. Man *et al.*, Deletion of adipocyte NOS3 potentiates high-fat diet-induced hypertension and vascular remodelling via chemerin. *Cardiovasc. Res.* **119**, 2755–2769 (2023). doi: 10.1093/cvr/cvad164; pmid: 37897505
28. O. Feron, F. Saldana, J. B. Michel, T. Michel, The endothelial nitric-oxide synthase-caveolin regulatory cycle. *J. Biol. Chem.* **273**, 3125–3128 (1998). doi: 10.1074/jbc.273.6.3125; pmid: 9452418
29. Z. Chen *et al.*, Reciprocal regulation of eNOS and caveolin-1 functions in endothelial cells. *Mol. Biol. Cell* **29**, 1190–1202 (2018). doi: 10.1091/mbc.E17-01-0049; pmid: 29563255
30. R. J. Lamb *et al.*, Hydropersulfides promote angiogenesis and preserve vascular function. *Redox Biol.* **94**, 104192 (2026). doi: 10.1016/j.redox.2026.104192; pmid: 42085865
31. D. Thuringer, L. Maulon, C. Frelin, Rapid transactivation of the vascular endothelial growth factor receptor KDR/Flk-1 by the bradykinin B2 receptor contributes to endothelial nitric-oxide synthase activation in cardiac capillary endothelial cells. *J. Biol. Chem.* **277**, 2028–2032 (2002). doi: 10.1074/jbc.M109493200; pmid: 11711543
32. D. J. Stuehr, M. M. Haque, Nitric oxide synthase enzymology in the 20 years after the Nobel Prize. *Br. J. Pharmacol.* **176**, 177–188 (2019). doi: 10.1111/bph.14533; pmid: 30402946
33. H. M. Abu-Soud, P. L. Feldman, P. Clark, D. J. Stuehr, Electron transfer in the nitric-oxide synthases. Characterization of L-arginine analogs that block heme iron reduction. *J. Biol. Chem.* **269**, 32318–32326 (1994). doi: 10.1016/S0021-9258(18)31638-7; pmid: 7528212
34. D. J. Stuehr *et al.*, Inhibition of macrophage and endothelial cell nitric oxide synthase by diphenyleneiodonium and its analogs. *FASEB J.* **5**, 98–103 (1991). doi: 10.1096/fasebj.5.1.1703974; pmid: 1703974
35. S. A. Everett, L. K. Folkes, P. Wardman, K. D. Asmus, Free-radical repair by a novel perthiol: Reversible hydrogen transfer and perthiyl radical formation. *Free Radic. Res.* **20**, 387–400 (1994). doi: 10.3109/10715769409145638; pmid: 8081454
36. T. Nakamura *et al.*, Integrated chemical and genetic screens unveil FSP1 mechanisms of ferroptosis regulation. *Nat. Struct. Mol. Biol.* **30**, 1806–1815 (2023). doi: 10.1038/s41594-023-01136-y; pmid: 37957306
37. A. C. Garcia, L. N. Zakharov, M. D. Pluth, Supramolecular activation of S_8 by cucurbiturils in water and mechanism of reduction to H_2S by thiols: Insights into biological sulfane sulfur trafficking. *J. Am. Chem. Soc.* **144**, 15324–15332 (2022). doi: 10.1021/jacs.2c06332; pmid: 35929817
38. S. S. Glasson, T. J. Blanchet, E. A. Morris, The surgical destabilization of the medial meniscus (DMM) model of osteoarthritis in the 129/SvEv mouse. *Osteoarthritis Cartilage* **15**, 1061–1069 (2007). doi: 10.1016/j.joca.2007.03.006; pmid: 17470400
39. Y. Xu *et al.*, Characteristics and time points to inhibit ferroptosis in human osteoarthritis. *Sci. Rep.* **13**, 21592 (2023). doi: 10.1038/s41598-023-49089-y; pmid: 38062071
40. X. Zhang *et al.*, Lipid peroxidation in osteoarthritis: Focusing on 4-hydroxynonenal, malondialdehyde, and ferroptosis. *Cell Death Discov.* **9**, 320 (2023). doi: 10.1038/s41420-023-01613-9; pmid: 37644030
41. M. Maemura *et al.*, Supersulfides contribute to joint homeostasis and bone regeneration. *Redox Biol.* **81**, 103545 (2025). doi: 10.1016/j.redox.2025.103545; pmid: 39983344
42. R. Shah, L. A. Farmer, O. Zilka, A. T. M. Van Kessel, D. A. Pratt, Beyond DPPH: Use of fluorescence-enabled inhibited autoxidation to predict oxidative cell death rescue. *Cell Chem. Biol.* **26**, 1594–1607.e7 (2019). doi: 10.1016/j.chembiol.2019.09.007; pmid: 31564533
43. M. Lange *et al.*, FSP1-mediated lipid droplet quality control prevents neutral lipid peroxidation and ferroptosis. *Nat. Cell Biol.* **27**, 1902–1913 (2025). doi: 10.1038/s41556-025-01790-y; pmid: 41162632
44. T. Zhang *et al.*, Enhanced cellular polysulfides negatively regulate TLR4 signaling and mitigate lethal endotoxin shock. *Cell Chem. Biol.* **26**, 686–698.e4 (2019). doi: 10.1016/j.chembiol.2019.02.003; pmid: 30853417
45. M. T. Hren, M. M. Tice, C. P. Chamberlain, Oxygen and hydrogen isotope evidence for a temperate climate 3.42 billion years ago. *Nature* **462**, 205–208 (2009). doi: 10.1038/nature08518; pmid: 19907491
46. Y. J. Taverne *et al.*, Reactive oxygen species: Radical factors in the evolution of animal life: A molecular timescale from Earth's earliest history to the rise of complex life. *BioEssays* **40**, 1700158 (2018). doi: 10.1002/bies.201700158; pmid: 29411901
47. B. Moosmann, M. Schindeldecker, P. Hajieva, Cysteine, glutathione and a new genetic code: Biochemical adaptations of the primordial cells that spread into open water and survived biospheric oxygenation. *Biol. Chem.* **401**, 213–231 (2020). doi: 10.1515/hsz-2019-0232; pmid: 31318686
48. H. H. Chen *et al.*, Expression of rat liver NAD(P)H:quinone-acceptor oxidoreductase in *Escherichia coli* and mutagenesis in vitro at Arg-177. *Biochem. J.* **284**, 855–860 (1992). doi: 10.1042/bj2840855; pmid: 1622401
49. S. Doll *et al.*, FSP1 is a glutathione-independent ferroptosis suppressor. *Nature* **575**, 693–698 (2019). doi: 10.1038/s41586-019-1707-0; pmid: 31634899
50. N. Kishi, Z. Li, K. Yoza, M. Akita, M. Yoshizawa, An M_2L_4 molecular capsule with an anthracene shell: Encapsulation of large guests up to 1 nm. *J. Am. Chem. Soc.* **133**, 11438–11441 (2011). doi: 10.1021/ja2037029; pmid: 21707060
51. N. Kishida, H. Sasafuchi, T. Sawada, M. Yoshizawa, Helicity control of a polyaromatic coordination capsule through stereoselective CH-π interactions. *Chem. Sci.* **15**, 13234–13239 (2024). doi: 10.1039/D4SC02103G; pmid: 39183906
52. K. Fukumoto, M. Yazaki, M. Arisawa, Rhodium-catalyzed synthesis of peptide polysulfides by insertion of sulfur into unprotected peptide disulfides. *Org. Lett.* **24**, 8176–8179 (2022). doi: 10.1021/acs.orglett.2c03257; pmid: 36317884
53. S. K. Bose, "Media for anaerobic growth of photosynthetic bacteria" in *Bacterial Photosynthesis*, H. Gest, A. San Pietro, L. P. Vernon, Eds. (Antioch Press, 1963), pp. 501–510.

54. T. Sato, K. Inoue, H. Sakurai, K. V. P. Nagashima, Effects of the deletion of *hup* genes encoding the uptake hydrogenase on the activity of hydrogen production in the purple photosynthetic bacterium *Rubrivivax gelatinosus* IL144. *J. Gen. Appl. Microbiol.* **63**, 274–279 (2017). doi: 10.2323/jgam.2017.01.003; pmid: 28904251
55. M. S. Longtine *et al.*, Additional modules for versatile and economical PCR-based gene deletion and modification in *Saccharomyces cerevisiae*. *Yeast* **14**, 953–961 (1998). doi: 10.1002/(SICI)1097-0061(199807)14:10<953::AID-YEA293>3.0.CO;2-U; pmid: 9717241
56. M. D. Krawchuk, W. P. Wahls, High-efficiency gene targeting in *Schizosaccharomyces pombe* using a modular, PCR-based approach with long tracts of flanking homology. *Yeast* **15**, 1419–1427 (1999). doi: 10.1002/(SICI)1097-0061(19990930)15:13<1419::AID-YEA466>3.0.CO;2-Q; pmid: 10509024
57. Y. Unno, T. Akuta, Y. Sakamoto, S. Horiuchi, T. Akaike, Nitric oxide-induced downregulation of leptin production by 3T3-L1 adipocytes. *Nitric Oxide* **15**, 125–132 (2006). doi: 10.1016/j.niox.2005.12.002; pmid: 16442319
58. D. L. Brasaemle, G. Dolios, L. Shapiro, R. Wang, Proteomic analysis of proteins associated with lipid droplets of basal and lipolytically stimulated 3T3-L1 adipocytes. *J. Biol. Chem.* **279**, 46835–46842 (2004). doi: 10.1074/jbc.M409340200; pmid: 15337753
59. T. Matsunaga *et al.*, Supersulphides provide airway protection in viral and chronic lung diseases. *Nat. Commun.* **14**, 4476 (2023). doi: 10.1038/s41467-023-40182-4; pmid: 37491435
60. L. J. Roman *et al.*, High-level expression of functional rat neuronal nitric oxide synthase in *Escherichia coli*. *Proc. Natl. Acad. Sci. U.S.A.* **92**, 8428–8432 (1995). doi: 10.1073/pnas.92.18.8428; pmid: 7545302
61. J. D. Fossetta *et al.*, Expression of human inducible nitric oxide synthase in *Escherichia coli*. *FEBS Lett.* **379**, 135–138 (1996). doi: 10.1016/0014-5793(95)01496-9; pmid: 8635578
62. B. M. Filippi *et al.*, Dynamin-related protein 1-dependent mitochondrial fission changes in the dorsal vagal complex regulate insulin action. *Cell Rep.* **18**, 2301–2309 (2017). doi: 10.1016/j.celrep.2017.02.035; pmid: 28273447
63. M. Bonora, K. Ito, C. Morganti, P. Pinton, K. Ito, Membrane-potential compensation reveals mitochondrial volume expansion during HSC commitment. *Exp. Hematol.* **68**, 30–37.e1 (2018). doi: 10.1016/j.exphem.2018.10.012; pmid: 30395909
64. R. E. Pauls, Determination of elemental sulfur in gasoline by gas chromatography with on-column injection and flame ionization detection following derivatization with triphenylphosphine. *J. Chromatogr. Sci.* **48**, 283–288 (2010). doi: 10.1093/chromsci/48.4.283; pmid: 20412650
65. D. Schilling *et al.*, Commonly used alkylating agents limit persulfide detection by converting protein persulfides into thioethers. *Angew. Chem. Int. Ed.* **61**, e202203684 (2022). doi: 10.1002/anie.202203684; pmid: 35506673
66. S. Asamitsu *et al.*, Supersulfide metabolome of exhaled breath condensate applied as diagnostic biomarkers for esophageal cancer. *Cancer Sci.* **116**, 1023–1033 (2025). doi: 10.1111/cas.16430; pmid: 39895210
67. B. Qiu, M. C. Simon, BODIPY 493/503 staining of neutral lipid droplets for microscopy and quantification by flow cytometry. *Bio Protoc.* **6**, e1912 (2016). doi: 10.21769/BioProtoc.1912; pmid: 28573161
68. J. Lu, S. Kunimoto, Y. Yamazaki, M. Kaminishi, H. Esumi, Kigamicin D, a novel anticancer agent based on a new anti-austerity strategy targeting cancer cells' tolerance to nutrient starvation. *Cancer Sci.* **95**, 547–552 (2004). doi: 10.1111/j.1349-7006.2004.tb03247.x; pmid: 15182438
69. P. Zhao *et al.*, Artificial lipid droplets: Novel effective biomaterials to protect cells against oxidative stress and lipotoxicity. *Nanomaterials* **12**, 672 (2022). doi: 10.3390/nano12040672; pmid: 35215001
70. W. Liu, N. A. Porter, C. Schneider, A. R. Brash, H. Yin, Formation of 4-hydroxynonenal from cardiolipin oxidation: Intramolecular peroxyl radical addition and decomposition. *Free Radic. Biol. Med.* **50**, 166–178 (2011). doi: 10.1016/j.freeradbiomed.2010.10.709; pmid: 21047551
71. M. J. Frisch *et al.*, Gaussian 09, Revision D.01 (Gaussian Inc., 2013).
72. T. Nakabayashi, K. Kosugi, N. Nishi, Liquid structure of acetic acid studied by Raman spectroscopy and Ab Initio molecular orbital calculations. *J. Phys. Chem. A* **103**, 8595–8603 (1999). doi: 10.1021/jp991501d
73. M. J. Abraham *et al.*, GROMACS: High performance molecular simulations through multi-level parallelism from laptops to supercomputers. *SoftwareX* **1–2**, 19–25 (2015). doi: 10.1016/j.softx.2015.06.001
74. J. B. Klauda *et al.*, Update of the CHARMM all-atom additive force field for lipids: Validation on six lipid types. *J. Phys. Chem. B* **114**, 7830–7843 (2010). doi: 10.1021/jp101759q; pmid: 20496934
75. S. R. Durell, B. R. Brooks, A. Ben-Naim, Solvent-induced forces between two hydrophilic groups. *J. Phys. Chem.* **98**, 2198–2202 (1994). doi: 10.1021/j100059a038
76. W. L. Jorgensen, J. Chandrasekhar, J. D. Madura, R. W. Impey, M. L. Klein, Comparison of simple potential functions for simulating liquid water. *J. Chem. Phys.* **79**, 926–935 (1983). doi: 10.1063/1.445869
77. D. Beglov, B. Roux, Finite representation of an infinite bulk system: Solvent boundary potential for computer simulations. *J. Chem. Phys.* **100**, 9050–9063 (1994). doi: 10.1063/1.466711
78. S. Jo, J. B. Lim, J. B. Klauda, W. Im, CHARMM-GUI Membrane Builder for mixed bilayers and its application to yeast membranes. *Biophys. J.* **97**, 50–58 (2009). doi: 10.1016/j.bpj.2009.04.013; pmid: 19580743
79. J. Lee *et al.*, CHARMM-GUI input generator for NAMD, GROMACS, AMBER, OpenMM, and CHARMM/OpenMM simulations using the CHARMM36 additive force field. *J. Chem. Theory Comput.* **12**, 405–413 (2016). doi: 10.1021/acs.jctc.5b00935; pmid: 26631602
80. L. Diedrich *et al.*, Energetics and kinetics of membrane permeation of photoresists for bioprinting. *Adv. Funct. Mater.* **34**, 2315731 (2024). doi: 10.1002/adfm.202315731
81. K. Vanommeslaeghe *et al.*, CHARMM general force field: A force field for drug-like molecules compatible with the CHARMM all-atom additive biological force fields. *J. Comput. Chem.* **31**, 671–690 (2010). doi: 10.1002/jcc.21367; pmid: 19575467
82. S. Kim *et al.*, CHARMM-GUI ligand reader and modeler for CHARMM force field generation of small molecules. *J. Comput. Chem.* **38**, 1879–1886 (2017). doi: 10.1002/jcc.24829; pmid: 28497616
83. S. Jo, T. Kim, V. G. Iyer, W. Im, CHARMM-GUI: A web-based graphical user interface for CHARMM. *J. Comput. Chem.* **29**, 1859–1865 (2008). doi: 10.1002/jcc.20945; pmid: 18351591
84. L. Seute, E. Hartmann, J. Stühmer, F. Gräter, Grappa – a machine learned molecular mechanics force field. *Chem. Sci.* **16**, 2907–2930 (2025). doi: 10.1039/D4SC05465B; pmid: 39822899
85. B. Hess, P-LINCS: A parallel linear constraint solver for molecular simulation. *J. Chem. Theory Comput.* **4**, 116–122 (2008). doi: 10.1021/ct700200b; pmid: 26619985
86. S. Miyamoto, P. A. Kollman, Settle: An analytical version of the SHAKE and RATTLE algorithm for rigid water models. *J. Comput. Chem.* **13**, 952–962 (1992). doi: 10.1002/jcc.540130805
87. S. Páll, B. Hess, A flexible algorithm for calculating pair interactions on SIMD architectures. *Comput. Phys. Commun.* **184**, 2641–2650 (2013). doi: 10.1016/j.cpc.2013.06.003
88. U. Essmann *et al.*, A smooth particle mesh Ewald method. *J. Chem. Phys.* **103**, 8577–8593 (1995). doi: 10.1063/1.470117
89. T. Darden, D. York, L. Pedersen, Particle mesh Ewald: An N·log(N) method for Ewald sums in large systems. *J. Chem. Phys.* **98**, 10089–10092 (1993). doi: 10.1063/1.464397
90. W. G. Hoover, Canonical dynamics: Equilibrium phase-space distributions. *Phys. Rev. A Gen. Phys.* **31**, 1695–1697 (1985). doi: 10.1103/PhysRevA.31.1695; pmid: 9895674
91. S. Nosé, A molecular dynamics method for simulations in the canonical ensemble. *Mol. Phys.* **52**, 255–268 (1984). doi: 10.1080/00268978400101201
92. H. J. C. Berendsen, J. P. M. Postma, W. F. van Gunsteren, A. DiNola, J. R. Haak, Molecular dynamics with coupling to an external bath. *J. Chem. Phys.* **81**, 3684–3690 (1984). doi: 10.1063/1.448118
93. M. Parrinello, A. Rahman, Polymorphic transitions in single crystals: A new molecular dynamics method. *J. Appl. Phys.* **52**, 7182–7190 (1981). doi: 10.1063/1.328693
94. W. Humphrey, A. Dalke, K. Schulten, VMD: Visual molecular dynamics. *J. Mol. Graph.* **14**, 33–38, 27–28 (1996). doi: 10.1016/0263-7855(96)00018-5; pmid: 8744570
95. R. J. Gowers *et al.*, "MDAnalysis: A python package for the rapid analysis of molecular dynamics simulations" in *Proceedings of the 15th Python in Science Conference* (2016), pp. 98–105.doi: 10.25080/Majora-629e541a-00e
96. N. Michaud-Agrawal, E. J. Denning, T. B. Woolf, O. Beckstein, MDAnalysis: A toolkit for the analysis of molecular dynamics simulations. *J. Comput. Chem.* **32**, 2319–2327 (2011). doi: 10.1002/jcc.21787; pmid: 21500218
97. N. Nitschke, K. Atkovska, J. S. Hub, Accelerating potential of mean force calculations for lipid membrane permeation: System size, reaction coordinate, solute-solute distance, and cutoffs. *J. Chem. Phys.* **145**, 125101 (2016). doi: 10.1063/1.4963192; pmid: 27782650
98. S. Kumar, J. M. Rosenberg, D. Bouzida, R. H. Swendsen, P. A. Kollman, THE weighted histogram analysis method for free-energy calculations on biomolecules. I. The method. *J. Comput. Chem.* **13**, 1011–1021 (1992). doi: 10.1002/jcc.540130812
99. J. S. Hub, B. L. de Groot, D. van der Spoel, g_wham—A free weighted histogram analysis implementation including robust error and autocorrelation estimates. *J. Chem. Theory Comput.* **6**, 3713–3720 (2010). doi: 10.1021/ct100494z
100. Y. Perez-Riverol *et al.*, The PRIDE database at 20 years: 2025 update. *Nucleic Acids Res.* **53**, D543–D553 (2025). doi: 10.1093/nar/gkae1011; pmid: 39494541

ACKNOWLEDGMENTS

The synthesis of PC and oPC was supported by R. Sumida and H. Sasafuchi (Institute of Science Tokyo). We thank K. Maisenbacher for the help with preparing the summary figure. **Funding:** This study was supported in part by Grants-in-Aid for Transformative Research Areas, International Leading Research, Scientific Research [(S), (A), (B), (C), Challenging Exploratory Research, Early-Career Scientists], Supporting Pioneering Research through AI for 1,000 Discovery challenges Program (SPReAD) from the Ministry of Education, Culture, Sports, Science and Technology (MEXT), Japan, to T.A. (JP21H05263, JP23K20040, JP24H00063, and JP22K19397), H.M. (JP21H05264, JP21H05258, and JP24H00605), T.T. (JP23K06094), S.O. (JP23K14333), M.J. (JP23K14341), T.M. (JP22K06893, JP25K03490, and 26K23340), M.M. (JP23K06145), T.Z. (JP26K17993 and JPMXP26282929), T.Sh. (JP21H05271, JP23KK0127, and JP25K09546), R.U. (JP21H05268 and JP23K23885), Y.U. (JP22K11796), M.A. (JP21K18947 and JP24H01322), L.C. (JSPS KAKENHI JP24H01311), and M.Y. (JP22H00348). This study was also supported in part by the Japan Science and Technology Agency (JST), CREST grant no. JPMJCR2024, Japan, to T.A., and the FOREST Program, grant no. JPMJFR205X, Japan, to M.A.; as well as a grant

from the Japan Agency for Medical Research and Development (AMED), grant no. JP21zf0127001, Japan, to T.A. and a Japan Society for the Promotion of Science (JSPS) fellowship to U.B. (PE23749). Research in the Olzmann lab is supported by a grant from the National Institutes of Health (NIH; R01CA305423) and Bakar Spark award to J.A.O. D.J.S. was supported by NIH grants R01GM130624 and R01GM148664. S.B., C.A.-S., and F.G. acknowledge support from the Klaus Tschira Foundation. T.P.D. acknowledges funding from the European Research Council (ERC, grant agreement no. 742039) and the German Research Council (DFG; SPP2306 and TRR186). M.C. received funding from the ERC under the European Union's Horizon 2020 research and innovation program (grant agreement no. GA 884754). N.X. and H.L. were supported by the DFG (project no. 407937360). **Author contributions:** U.B. and T.T. contributed MS analysis for quantification of S_8. L.C. and M.Y. contributed optimization of PC and oPC for capturing S_8. T.Sh., A.N., and M.M. contributed to the construction of bacterial and yeast mutants. M.M., M.J., and T.M. performed mitochondria purification. R.U. contributed to the fractionation of cellular organelle. M.J., Y.U., and S.N. contributed Raman analysis for detection of S_8. T.N. contributed DFT calculations of supersulfide and polysulfide structures. T.Is. and N.T. collected exhaled breath condensate samples and informed consent from patients with breast cancer. S.A., K.F., T.Su., and T.Is. contributed to the collection of human tissues and LD isolation. S.O., T.Id., and T.Z. performed proteome analysis of LDs. S.O., T.T., T.Id., and T.Z. performed the supersulfide and polysulfide metabolome anaylsis. N.X. and H.L. provided the eNOS-CKO adipose tissue samples. Y.W. and Y.T. supplied recombinant eNOS. T.T. performed recombinant eNOS-mediated sulfur catenation experiments. M.A. contributed to the synthesis of trisulfide derivatives. P.G. contributed to the AlphaFold prediction. M.J. and Y.P. performed colocalization experiments for mitochondria and LD. Y.U., M.J., and Y.P. performed LPO experiments with adipocytes and chondrocytes. M.L. performed LPO experiments. S.B., F.G., and C.A.S. performed MD simulations. F.Y., S.O., and T.T. contributed OA model experiments. U.B., Y.W., R.Y., A.v.d.V., D.J.S., J.A.O., B.M., E.M., M.C., T.P.D., H.M., M.Y., and T.A. provided technical advice and valuable interpretations of supersulfide and polysulfide chemistry and the experimental results. T.A. supervised and coordinated the study. U.B. and T.A. designed the study and guided the experimental design and analysis. U.B., T.A., T.M., M.M., H.M., E.M., M.C., and T.P.D. wrote the manuscript with input from all authors. **Competing interests:** M.C. holds patents for some of the compounds described herein. J.A.O. consults for Dojindo and has pending patent applications related to ferroptosis targeting. B.M. holds a patent on alkyl thiols as ferroptosis inducers. J.A.O. is an inventor on patent application US20250161297A1/EP4486461A2, submitted by The Regents of the University of California, which covers compositions and methods for inhibiting FSP1. The other authors declare no competing interests. **Data, code, and materials availability:** All data supporting the findings of this study are available within the paper and its supplementary materials. The MS proteomics data have been deposited to the ProteomeXchange Consortium via the PRIDE (*100*) partner repository with the dataset identifier PXD080540, and code for MD simulations can be found under the following link: https://github.com/saberBoushehri/Octasulfur-MD. Alphafold 3 models of the NOS reductase domain in complex with ligands $FADH_2$, FMN, BH_4, and GSSSG are available at https://github.com/PaulGreic/NOS-reductase-domain-in-complex-with-ligands. Correspondence and requests for materials should be addressed to corresponding author T.A. **License information:** Copyright © 2026 the authors, some rights reserved; exclusive licensee American Association for the Advancement of Science. No claim to original US government works. https://www.science.org/about/science-licenses-journal-article-reuse. This research was funded in whole or in part by the ERC (742039, GA 884754, and 407937360) and the DFG (SPP2306 and TRR186); as required, the author will make the Author Accepted Manuscript (AAM) version available under a CC BY public copyright license.

SUPPLEMENTARY MATERIALS

science.org/doi/10.1126/science.aec5473
Figs. S1 to S26; Tables S1 and S2; Data S1 and S2; Reference (*101*);
MDAR Reproducibility Checklist

Submitted 28 September 2025; accepted 23 July 2026

10.1126/science.aec5473

Copyright 2026 American Association for the Advancement of Science. All rights reserved.